



## Article

# Mapping Alteration Mineralogy in Eastern Tsogttsetsii, Mongolia, Based on the WorldView-3 and Field Shortwave-Infrared Spectroscopy Analyses

Young-Sun Son <sup>\*</sup>, Byoung-Woon You, Eun-Seok Bang, Seong-Jun Cho, Kwang-Eun Kim, Hyunseob Baik and Hyeong-Tae Nam

Korea Institute of Geoscience and Mineral Resources, Daejeon 34132, Korea; ybw8217@kigam.re.kr (B.-W.Y.); esbang@kigam.re.kr (E.-S.B.); mac@kigam.re.kr (S.-J.C.); kimke@kigam.re.kr (K.-E.K.); hsbaik@kigam.re.kr (H.B.); nht@kigam.re.kr (H.-T.N.)

\* Correspondence: sys6564@kigam.re.kr

**Abstract:** This study produces alteration mineral maps based on WorldView-3 (WV-3) data and field shortwave-infrared (SWIR) spectroscopy. It is supported by conventional analytical methods such as X-ray diffraction, X-ray fluorescence, and electron probe X-ray micro analyzer as an initial step for mineral exploration in eastern Tsogttsetsii, Mongolia, where access is limited. Distributions of advanced argillic minerals (alunite, dickite, and kaolinite), illite/smectite (illite, smectite, and mixed-layered illite-smectite), and ammonium minerals (buddingtonite and NH<sub>4</sub>-illite) were mapped using the decorrelation stretch, band math, and mixture-tuned-matched filter (MTMF) techniques. The accuracy assessment of the WV-3 MTMF map using field SWIR data showed good WV-3 SWIR data accuracy for spectrally predominant alteration minerals such as alunite, kaolinite, buddingtonite, and NH<sub>4</sub>-illite. The combination of WV-3 SWIR mineral mapping and a drone photogrammetric-derived digital elevation model contributed to an understanding of the structural development of the hydrothermal system through visualization of the topographic and spatial distribution of surface alteration minerals. Field SWIR spectroscopy provided further detailed information regarding alteration minerals such as chemical variations of alunite, crystallinity of kaolinite, and aluminum abundance of illite that was unavailable in WV-3 SWIR data. Combining WV-3 SWIR data and field SWIR spectroscopy with conventional exploration methods can narrow the selection between deposit models and facilitate mineral exploration.

**Keywords:** high sulfidation alteration mineral; WorldView-3; field spectroscopy; shortwave-infrared; Mongolia



**Citation:** Son, Y.-S.; You, B.-W.; Bang, E.-S.; Cho, S.-J.; Kim, K.-E.; Baik, H.; Nam, H.-T. Mapping Alteration Mineralogy in Eastern Tsogttsetsii, Mongolia, Based on the WorldView-3 and Field Shortwave-Infrared Spectroscopy Analyses. *Remote Sens.* **2021**, *13*, 914. <https://doi.org/10.3390/rs13050914>

Academic Editors: Olga Sykioti, Konstantinos Koutroumbas and Amin Beiranvand Pour

Received: 31 December 2020

Accepted: 24 February 2021

Published: 1 March 2021

**Publisher's Note:** MDPI stays neutral with regard to jurisdictional claims in published maps and institutional affiliations.



**Copyright:** © 2021 by the authors. Licensee MDPI, Basel, Switzerland. This article is an open access article distributed under the terms and conditions of the Creative Commons Attribution (CC BY) license (<https://creativecommons.org/licenses/by/4.0/>).

## 1. Introduction

Porphyry Cu deposits are mostly found in magmatic arcs associated with subduction zones, and are generated by hydrothermal fluid processes which accompany porphyry emplacement and alter the mineralogy and geochemistry of the host rocks. In general, the movement of these hydrothermal fluids generates broad-scale alteration zones. These alteration zones are composed of sodic-calcic, potassic, propylitic, chlorite-sericite, sericitic (phyllitic), and advanced argillic, which are characterized by the occurrence of specific mineral assemblages [1–3].

The shortwave-infrared (SWIR) wavelength region (~1.4 to 3.0 μm) provides information about the specific spectral absorption of hydrothermal alteration minerals associated with porphyry Cu or epithermal deposits [4–6]. SWIR data are particularly useful for mineral mapping in areas that are difficult to access owing to environmental or geographical reasons [7–9]. These data have been used effectively for detecting the spatial distribution of alteration zones associated with porphyry Cu deposits [4,5,10–12]. A sensor on board the eighth Landsat satellite, the Operational Land Imager (OLI), has two SWIR bands ranging

from wavelengths 1.57 to 2.29  $\mu\text{m}$ , and a spatial resolution of 30 m (Table 1). The Landsat SWIR bands facilitate extensive mapping of well-exposed hydrothermally altered rocks, based mainly on the intense absorption feature in the 2.2  $\mu\text{m}$  region related to alteration minerals. However, the two bands cannot distinguish between alteration minerals which have similar spectral absorption positions (e.g., argillic and phyllic minerals) [10,13]. The Advanced Spaceborne Thermal Emission and Reflection Radiometer (ASTER) has six SWIR bands, ranging between 1.60 and 2.43  $\mu\text{m}$  with a spatial resolution of 30 m. Previous studies have shown that ASTER SWIR bands are capable of separating advanced argillic minerals (alunite, kaolinite, dickite, pyrophyllite), phyllic alteration minerals (sericite, and illite), and propylitic minerals (carbonate, epidote, and chlorite) [4,5,9,13–15]. The spatial resolution of 30 m per pixel does, however, limits the detailed mapping of the spatial distribution of minerals [16]. Crosstalk phenomenon occurring in ASTER SWIR bands (especially in band 4 centered at 1.65  $\mu\text{m}$  and band 9 centered at 2.395  $\mu\text{m}$ ) can cause the misclassification of some minerals, for example, alunite and kaolinite [17]. Several correction methods have been proposed [17–19], but this phenomenon has not been completely corrected. The WorldView-3 (WV-3) consists of eight SWIR bands ranging between 1.195 and 2.365  $\mu\text{m}$ , with a current maximum spatial resolution of 3.7 m. Several studies have shown that WV-3 allows more detailed mineral and lithologic mapping compared to Landsat OLI and ASTER [16,20]. The WV-3 data have been effective in mineral mapping in areas associated with hydrothermal alteration deposit, such as Cuprite Hills and Mountain Pass in the USA [21,22], Zefreh, in Iran [23], and the Rodalquilar caldera, in Spain [24].

**Table 1.** Performance characteristics of WV-3, Terra/ASTER, and Landsat-8/OLI [8,16,24].

Satellite/Sensor	SWIR Band No.	Spectral Range ( $\mu\text{m}$ )	Spatial Resolution
WorldView-3	SWIR-1	1.195–1.225	3.7 m
	SWIR-2	1.550–1.590	
	SWIR-3	1.640–1.680	
	SWIR-4	1.710–1.750	
	SWIR-5	2.145–2.185	
	SWIR-6	2.185–2.225	
	SWIR-7	2.235–2.285	
	SWIR-8	2.295–2.365	
Terra/ASTER	4	1.600–1.700	30 m
	5	2.145–2.185	
	6	2.185–2.225	
	7	2.235–2.285	
	8	2.295–2.365	
Landsat-8/OLI	6	1.560–1.660	30 m
	7	2.100–2.300	

Several techniques, such as band math (BM), decorrelation stretch (DS), and principle component analysis (PCA), have been used for a long time to produce iron oxide and hydroxyl images that may be related to hydrothermal alteration and to highlight alteration zones [5,10,13,22]. The methods of spectral angle mapper (SAM), matched filtering (MF), mixed-tuned-matched filter (MTMF), and Adaptive Coherence Estimator (ACE) have been widely used in multispectral images for mapping individual hydrothermal alteration minerals [4,8,9,11,21,23,24]. Recently, the use of machine learning algorithms such as artificial neural network (ANN), support vector machine (SVM), and extreme learning machine (ELM) for the mineral identification in remote sensing images is increasing [25–27],

but most of them are applied to laboratory-based hyperspectral images or spectra, and they are rarely used for the mineral identification in multispectral images [28].

A number of Paleozoic porphyry Cu occurrences and deposits, mainly associated with Devonian to Carboniferous subduction-related magmatism, were discovered in southeastern Gobi, Mongolia, for example, Tsagaan Suvrga, Oyu Tolgoi, Ikh-Shankhai, Kharmagtai, and Shuteen [29–32]. Son et al. [12] identified hydrothermal alteration anomalies, using the Landsat Enhanced Thematic Mapper Plus and ASTER, in eastern Tsogttsetsii adjacent to the Ikh-Shankhai porphyry Cu deposit Mongolia. However, due to the harsh weather and low accessibility, there was no field verification and detailed mineral mapping for hydrothermal alteration anomalies in eastern Tsogttsetsii in the previous study. In addition, there is an absence of other similar publications that address this area.

The purpose of this study is to show how information from WV-3 SWIR data can be used with other conventional analytical methods such as X-ray diffraction (XRD), X-ray fluorescence (XRF), and electron probe X-ray micro analyzer (EPMA) for mineral exploration in an unknown area. Recent WV-3 studies on hydrothermal mineral mapping have focused more on evaluating instrument performance and analytical techniques in well-known areas [16,21–24], and less focused on interpretation of hydrothermal systems and deposit models in unknown areas. Our study presents further investigation locations in eastern Tsogttsetsii that may be related to the intrusion center of deposit. Drone-based digital elevation model (DEM) data, alongside the WV-3 SWIR surface mineral mapping, was used to topographically and structurally identify the distribution of hydrothermal alteration minerals, and discern the details of alteration zoning. This study also assesses the performance of WV-3 SWIR bands in mapping hydrothermal alteration minerals at eastern Tsogttsetsii.

## 2. Geologic and Field Observations

The eastern Tsogttsetsii is a semi-arid desert with an annual precipitation of approximately 50–100 mm and sparse vegetation. The area has a flat terrain with an elevation ranging from 1460 to 1595 m, with some scattered hilly outcrops composed of volcanic rock and intrusive granite. There are advantages in mapping hydrothermal alteration minerals in magmatic-hydrothermal ore deposits using optical remote sensing techniques [33]. The eastern Tsogttsetsii has a basement of volcano-sedimentary rocks, intruded by plutonic and subvolcanic rocks during the Carboniferous to the Permian (Figure 1). In turn, clastic sedimentary rocks were deposited from the Cretaceous to the Quaternary.

The study area (Figure 1) is comprised of andesitic to basaltic tuffaceous sedimentary rocks of the Doshinn-Ovoo Formation, and rhyolitic to andesitic tuff of the Argalant Formation. The Upper Carboniferous Doshinn-Ovoo Formation crops out throughout the southern part of the study area and is intruded by subvolcanic rocks of the Permian age. The subvolcanic rocks, which are rhyodacite and trachyrhyodacite in composition, include hydrothermal alteration minerals.

This study focuses on three hydrothermal alteration zones (Figures 1 and 2). The advanced argillic alteration zone in Prospect I was divided into the southern and northwestern parts according to the trending direction. The southern part trends in a north–south (NS) direction with a dip to N30°E (Figure 3a). In the southern part of Prospect I, quartz–alunite–dickite–kaolinite is dominant, and is associated with breccias and vuggy quartz in the core zone. In the zone below, banded quartz–dickite–kaolinite and hematite layers are dominant (Figure 3b–d). The northwestern part strikes towards N40°W with a dip in the southern direction (Figures 2 and 3e). The northernmost part of the alteration zone is composed of a quartz–alunite–dickite alteration. Varying degrees of breccia and several stages of alunite were observed (Figure 3f). Alunite veins are a cut, well-bedded pervasive hydrothermal alteration (Figure 3g). The lower zone consists of a massive coarse-grained dickite–kaolinite alteration (Figure 3f,h,i).

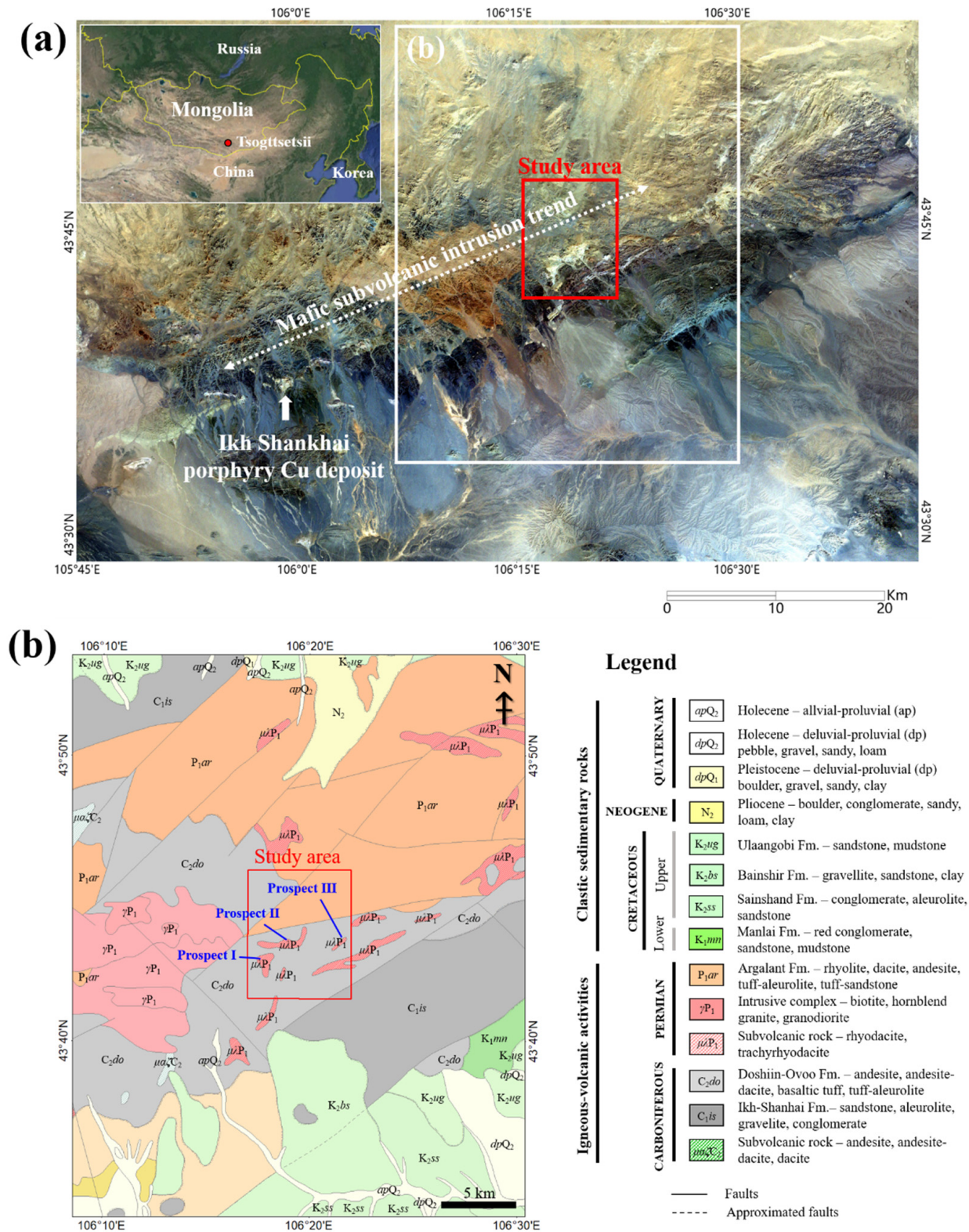


**Figure 1.** (a) Landsat Enhanced Thematic Mapper Plus image showing the location of Ikh shkhai porphyry Cu deposit and study area; and (b) geological map of the eastern Tsogttsetsii (modified from [34]). Inner map in (a) shows the location of Mongolia and Tsogttsetsii. The red lines define the study area corresponding to Figure 2.

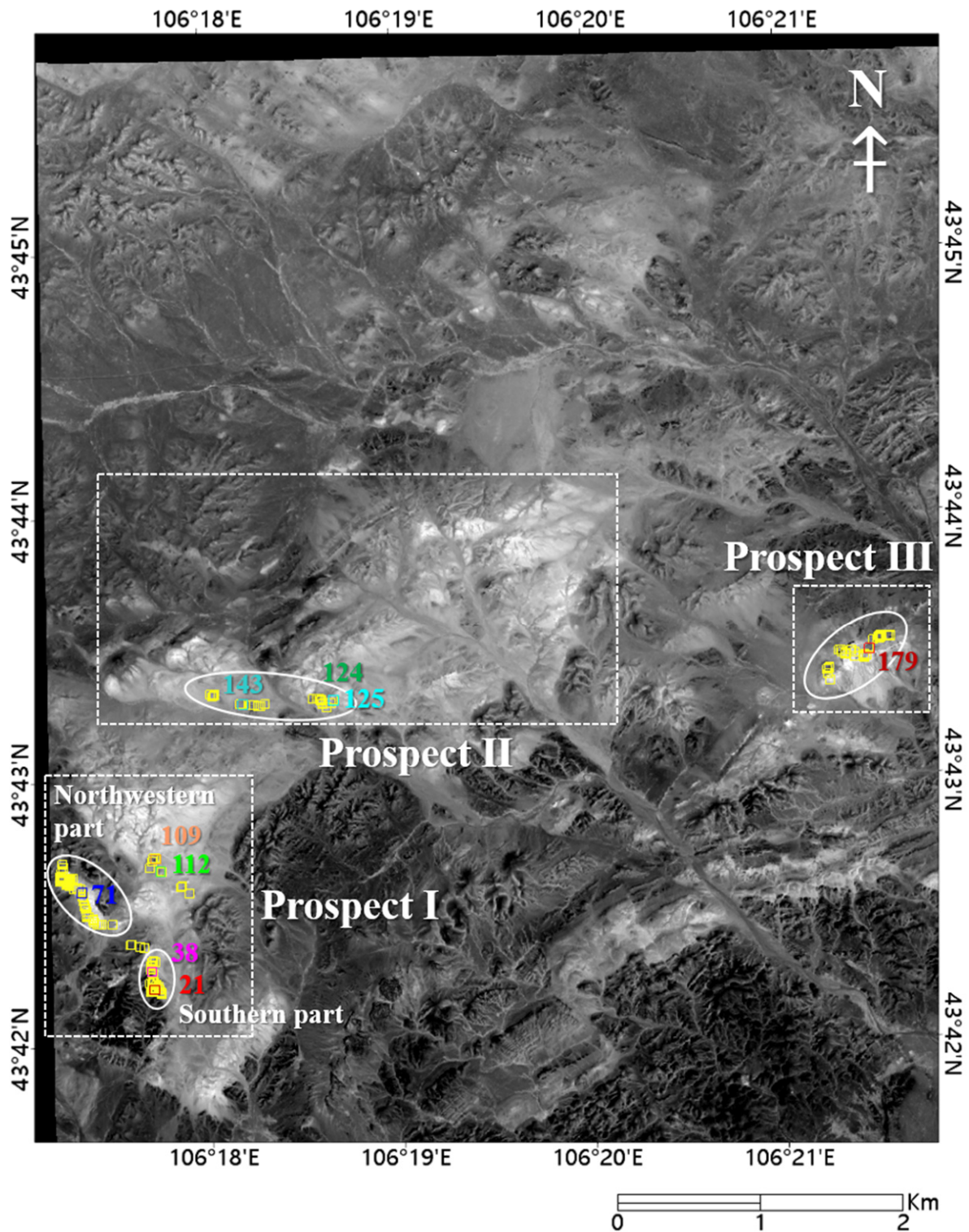


**Figure 2.** WorldView-3 (WV-3) shortwave-infrared (SWIR) band 1 image of eastern Tsogttsetsii, Mongolia showing the location of field spectral measurements and rock sampling (yellow squares). Acquisition locations of representative field reflectance spectra shown in Figure 4 are indicated by numbers and colors. The dashed white squares indicate the location of three main zones of hydrothermal alteration: Prospects I, II, and III. White solid line circles display the main trending direction of alteration zones. Bright areas in the image correspond to subvolcanic rocks and bleached rocks, and dark areas correspond to basaltic rocks.



**Figure 3.** Photographs of rocks in the prospects of the study area. Prospect I: (a) quartz–alunite–dickite–kaolinite–hematite alteration of the southern part; (b) enlarged part of Figure 3a showing the upper part with quartz–alunite–dickite–kaolinite assemblages and the lower part with quartz–dickite–kaolinite–hematite assemblages; (c) a rock sample (TS117) showing alunite–kaolinite and dickite–alunite breccia and vuggy quartz in the upper part of Figure 3b; (d) banded quartz–dickite–kaolinite and hematite layers in the lower part of Figure 3b; (e) the northern alteration zone in the N40°W direction, unlike the southern alteration zone in the NS direction; (f) the northernmost part of the northern alteration zone, where breccia and well-bedded quartz–dickite–kaolinite alteration border; (g) a rock sample (TS140) from the upper part of Figure 3f showing an alunite vein that cuts the well-bedded quartz–dickite–kaolinite; (h) a rock sample (TS139) from the lower well-bedded quartz–dickite–kaolinite alteration of Figure 3f; and (i) a rock sample (TS138) collected from a massive coarse dickite–kaolinite layer, approximately 1 m thick, located in the middle of the alteration zone. Prospect II: (j) remnant volcanic rocks and eastern hydrothermal alteration zones; (k) alternation of chalcedony quartz and dickite; (l) massive vuggy quartz–dickite–kaolinite and dickite–kaolinite–hematite alterations in the center of the hydrothermal alteration zone; and (m) alunite breccia with hematite matrix found in the easternmost part. Prospect III: (n) connecting part of the quartz–kaolinite–dickite–alunite alteration and the quartz–kaolinite–dickite–alunite–hematite alteration zone; (o) a rock sample (TS121) showing elliptical dickite patches and flow textures; (p) remnants of basaltic volcanic rocks in the northeast; (q) filled dickite–kaolinite–alunite within relatively large gas cavities; (r) filled dickite–kaolinite within fine gas cavities; (s) remnants and relicts of basaltic tuff.

The hydrothermal alteration zone at Prospect II trends in an almost east–west direction and is characterized by extensive bleaching zones (Figures 2 and 3j). The brecciation and pervasive dickite alterations are common in the center of the alteration zone. Massive vuggy quartz–dickite–kaolinite alteration predominates and is partly oxidized (Figure 3k,l). The quartz–alunite was brecciated, and a hematite matrix was also observed (Figure 3m).

The hydrothermal alteration zone at Prospect III is approximately 500 m long and 300 m wide. It strikes northeast and dips to the southeast ( $\sim 30^\circ$ ) (Figure 2). The Prospect III consists of predominantly quartz–kaolinite–dickite–alunite assemblages, and hematite was observed due to the oxidation of sulfides at the top (Figure 3n). Below the quartz–kaolinite–dickite–alunite zone, a massive dickite alteration is dominant and is well preserved with flow foliation by dickite patches of the volcanic rock (Figure 3o). In the western part of the hill, relicts of basaltic tuff are common (Figure 3p,q). A dickite–kaolinite–alunite alteration fills the cavities of the basaltic tuff (Figure 3r), whilst a dickite–kaolinite alteration replaces plagioclase phenocrysts (Figure 3s).

### 3. Methods

#### 3.1. Field Reflectance Spectrum Measurements

Field spectra and rock sample acquisition was conducted from 21–27 July 2018, to map the hydrothermal alteration mineralogy and to evaluate the performance of the WV-3 SWIR data. Field spectra were used to obtain further detailed information regarding alteration minerals that was unavailable in WV-3 SWIR data. A total of 192 field reflectance spectra of the rock outcrops, and 35 rock samples, were collected in the three hydrothermal alteration zones (Figure 2) identified from the ASTER analysis in our previous study [12]. Field reflectance spectra were collected along the trending direction of lithocaps that were not covered with soil and vegetation identified in field observation (Figure 3). There were measured using a portable analytical spectral device (ASD) TerraSpec Halo mineral identifier, which records 2151 channels spanning a spectral range of 0.35–2.5  $\mu\text{m}$  (<https://www.malvernpanalytical.com/en/products/product-range/asd-range/>) (accessed on 31 December 2020). In this study, only the SWIR wavelength region (1.1–2.4  $\mu\text{m}$ ) corresponding to the WV-3 SWIR bands was used. Mineral identification was manually conducted by comparing the wavelength position of the absorption features and the general shape of the continuum removed field SWIR spectra with United States Geological Survey (USGS) spectral libraries and various studies [4,35–40]. The results from the field SWIR spectral analysis were cross-checked with those obtained via conventional laboratory methods such as XRD, XRF, and EPMA. A confusion matrix showing the statistics of the classification accuracy such as the kappa index and overall accuracy [41] was used to evaluate errors between the ground reference data and image classification.

#### 3.2. Chemical Analysis

Mineralogical identification in the rock samples was performed using an X-ray diffractometer (X'Pert MPD, Philips) at the Korea Institute of Geoscience and Mineral Resources (KIGAM). The diffractometer was done at 40 kV and 25 mA. Randomly orientated specimens were continuously scanned in the range of  $3^\circ$ – $70^\circ$   $2\theta$  using Cu K-alpha radiation. The detection limit was 1 wt.%. XRF analyses used a Shimadzu MXF-2400 at KIGAM. Glass discs were prepared using a lithium tetraborate flux ( $\text{Li}_2\text{B}_4\text{O}_7$ ) mixture at  $1100^\circ\text{C}$  for 10 minutes. EPMA analyses of alunite, dickite–kaolinite, pyrophyllite, and illite/muscovite field samples were conducted using a JEOL JXA-8530F Electron Microprobe operated at Gyeongsang National University. The analysis conditions were acceleration voltage 15 kV, beam current 20 nA, and spot size 1  $\mu\text{m}$ .

### 3.3. WV-3 SWIR Data Preprocessing

The cloud-free WV-3 level-2A SWIR data was acquired two days prior to the commencement of the field survey, on July 19, 2018. Although the WV-3 SWIR bands had an initial spatial resolution of 3.7 m, the WV-3 SWIR data in this study had a spatial resolution of 7.5 m due to United States governmental restrictions.

The WV-3 SWIR data were converted to top-of-atmosphere radiance using the following formula [42]:

$$L = \text{Gain} * \text{DN} * (\text{ACF}/\text{EB}) + \text{Offset} \quad (1)$$

where  $L$  is the top-of-atmosphere radiance in  $\text{W}\mu\text{m}^{-1}\text{m}^{-2}\text{sr}^{-1}$ , and the Gain and Offset are the absolute radiometric calibration band dependent adjustment factors for WV-3 SWIR, used for more accurate sensor radiance values. In this study, the calibration adjustment factors released in the 2018 vicarious version were used [43]. The absolute calibration factor (ACF) in  $\text{Wm}^{-2}\text{sr}^{-1}$  and the effective bandwidth (EB) in  $\mu\text{m}$  were delivered in the metadata file. The digital number (DN) is the pixel value in the imagery. The WV-3 SWIR top-of-atmosphere radiance data were converted to reflectance data using internal average relative reflectance (IAR) calibration, that eliminates the majority of atmospheric effects [44]. The relative reflectance was calculated by determining an average spectrum for the WV-3 SWIR data and dividing each spectrum in the data by the average spectrum. The IAR calibration has been effective for the mapping of mineral distribution, especially in arid or semi-arid areas with no vegetation, such as this study region [45–47].

The quality of reflectance calibration was verified by comparing the WV-3 SWIR reflectance image spectra with field reflectance spectra. Figure 4 compares the field reflectance spectra of representative minerals in the study area and reflectance spectra derived from single WV-3 SWIR image pixel at the same locations. For comparison, field reflectance spectra (160 bands between 1.195 and 2.365  $\mu\text{m}$ ), were resampled to WV-3 SWIR bandpass wavelengths (8 bands between 1.195 and 2.365  $\mu\text{m}$ ). Spectral resampling was conducted using ENVI software, which uses a Gaussian model using the wavelengths and full width at half maximum (FWHM) spacing. Figure 4 shows a good match between the WV-3 SWIR spectra and resampled field reflectance spectra at the same location.

### 3.4. WV-3 SWIR Data Mapping

#### 3.4.1. Decorrelation Stretch and Band Math

Decorrelation stretch (DS) and band math (BM) were used to map lithologic units and alteration zones by highlighting spectral characteristics related to chemical composition prior to conducting more detailed, time-consuming MTMF. These results were validated with a geologic map, field observations, and field spectral measurements. The DS removes the high correlation commonly found in multispectral imagery, and quickly and easily emphasizes spectral reflectance differences attributable to mineralogical variation [48,49]. Band math techniques, such as relative absorption-band depth [50,51] and the mineralogic index [52] highlight the Al-OH, Fe, Mg-OH, and  $\text{CO}_3$  absorption features of minerals and rocks, while reducing the effects related to albedo and topographic slope variations. In general, the denominator is assigned to the minimum reflectance band for each absorption feature, and the reflectance band representing the shoulders is assigned to the numerator. Higher values in the histogram of the BM image reflect absorption feature close to those of the mineral, and the threshold is generally determined empirically in the image [51,52]. In this study, the threshold was determined by referring to the alteration zones observed in the field survey.

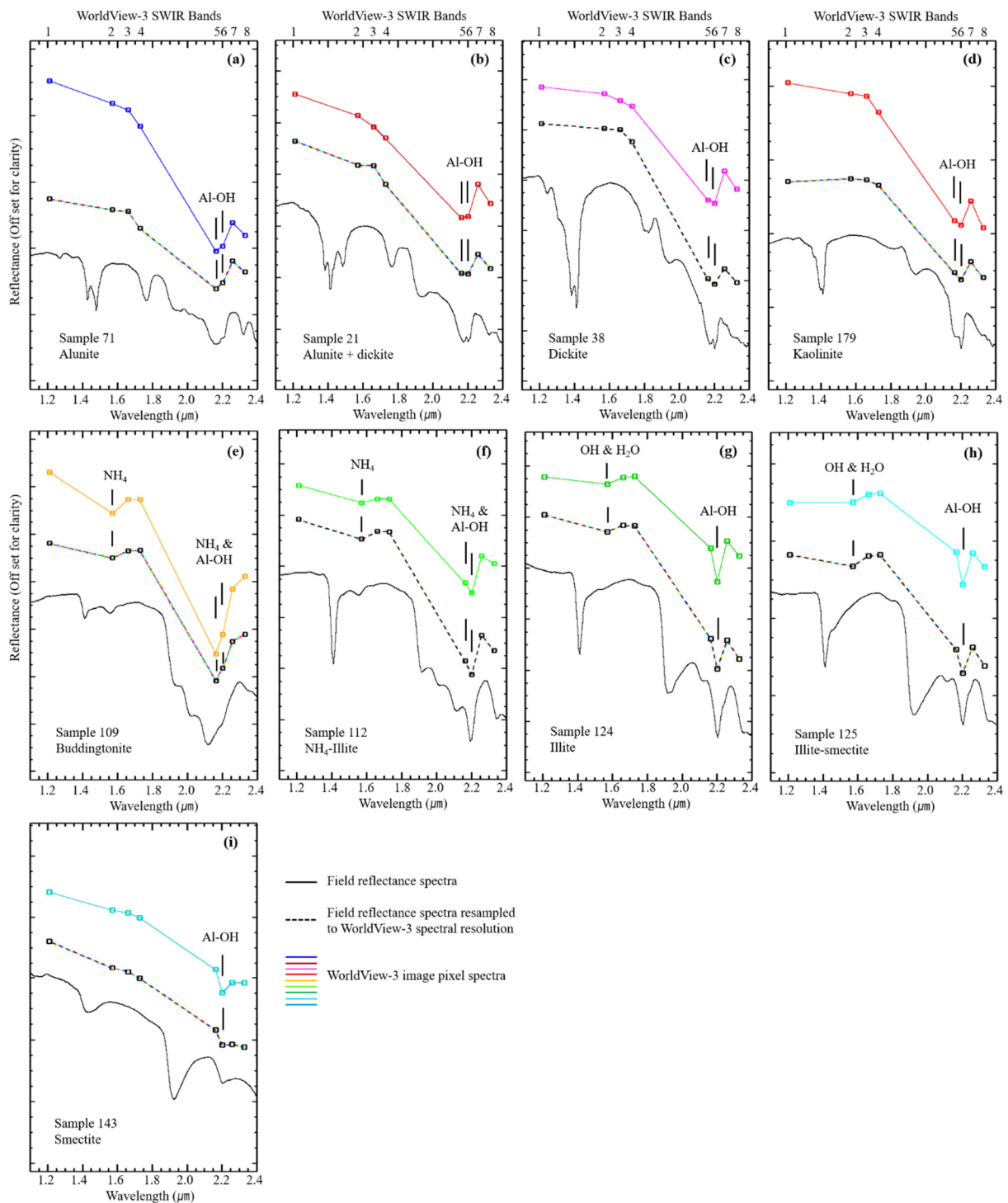


**Figure 4.** Comparison of field reflectance spectra of representative minerals in the study area resampled to the spectral resolution of WV-3 SWIR (black dashed lines), with WV-3 SWIR pixel spectra (solid lines with color) at the same locations. Square symbols show WV-3 SWIR band centers. Black vertical solid lines indicate wavelength positions of absorption features for NH<sub>4</sub>, OH, H<sub>2</sub>O, and Al-OH. Locations of field spectra are shown in Figure 2 with sample numbers. Note that a satellite pixel was assumed to be a spectrally predominant class.

### 3.4.2. Mixture-Tuned-Matched Filter

The MTMF was applied to the WV-3 SWIR data to map the distribution of exposed hydrothermal alteration minerals in the study area. Unlike general spectral unmixing methods, the MTMF is a partial unmixing technique that does not require all spectral endmembers for full background composition. This is used to map the apparent abundance of a known target material in the presence of mixed and unknown background components [20]. It was developed to mitigate the issue of false alarms that occurred for lower abundances arising from the use of the matched filter (MF) approach [53]. This allows the determination of specific minerals and the estimation of their pixel abundances by calculating the MF and infeasibility score. A high MF score indicates a high contribution of the endmember spectrum, for example, known target mineral, to each unknown spectrum in the scene. The infeasibility score indicates the likelihood that the spectrum may be a linear mixture of the endmember spectrum at a certain abundance, and the background distribution. Pixels with high infeasibility scores are rejected because they are likely to be MF false positives that represent physically unreasonable mixtures. Pixels with high MF scores and low infeasibility are selected [20]. In general, a user interactively sets a threshold using a 2D scatter plot that is set as an infeasibility score for the MF score [54,55].

### 3.5. Drone Photogrammetric-Derived DEM

The study area is large, and we therefore, selected Prospect I, with the most widespread advanced argillic zone, and used a Dà-Jiāng Innovations' (DJI's) Inspire2 drone with a Zennuse X7 24 mm lens to take the photograph. The target area was approximately 2 km in the east–west and north–south directions. Although there are hills and rocky outcrops, the area is generally flat, and photographs were acquired by automatic flight at an altitude of 150 m with an 80% horizontal and 60% vertical image overlap. Through the photo merge, and considering the location of the photography, an orthophoto with a 2.67 cm spatial resolution per pixel was derived and a DEM was created using the Agisoft Photoscan program ([https://www.agisoft.com/pdf/photoscan-pro\\_1\\_4\\_en.pdf](https://www.agisoft.com/pdf/photoscan-pro_1_4_en.pdf)) (accessed on 31 December 2020).

## 4. Results

### 4.1. Field Shortwave-Infrared Spectroscopy

The field SWIR reflectance spectra collected at the prospects of the eastern Tsogttsetsii were characterized by absorption features indicating the presence of advanced argillic alteration minerals (alunite, dickite, kaolinite), buddingtonite,  $\text{NH}_4$ -illite, illite, smectite, and mixed-layered illite-smectite (Figure 4; Table A1). Although XRD analysis and field verification show quartz and hematite in the prospects (Figure 3; Table A1), these minerals typically do not have diagnostic spectral features at SWIR [51,52].

Alunite from the study area exhibited absorption features near 1.429 and 1.479  $\mu\text{m}$ , which was attributed to the doublet OH absorption, and at 2.165  $\mu\text{m}$ , which was attributed to Al-OH absorption (Figure 5b). Alunite is an important component of advanced argillic alteration in high sulfidation deposits [1]. The alunite spectrum was commonly identified in Prospect I, but it was relatively less frequently identified in Prospects II and III (Table A1). Many field spectra samples indicate that alunite is mixed with dickite and kaolinite (Figure 5b). This was supported by XRD, petrographic, and EPMA analysis (Figures 6a and 7a; Table A1). Chemical variations between K and Na-bearing alunite  $[(\text{K},\text{Na})\text{Al}_3(\text{SO}_4)_2(\text{OH})_6]$  shift the location of the OH overtone doublet absorptions at 1.429 and 1.479  $\mu\text{m}$  (Figure 8a). As Na content increases, the OH overtone doublet absorption in the K-alunite spectrum shifts to longer wavelengths. The position of the 1.479  $\mu\text{m}$  absorption was strongly controlled by the composition and can be used to calculate the mole fraction of Na ( $X_{\text{Na}}$ ) [33]:

$$X_{\text{Na}} = 0.2974 (-\ln((0.0281/(\lambda - 1.4705)) - 1)) + 0.3632 (1.477 < \lambda < 1.496 \mu\text{m}) \quad (2)$$

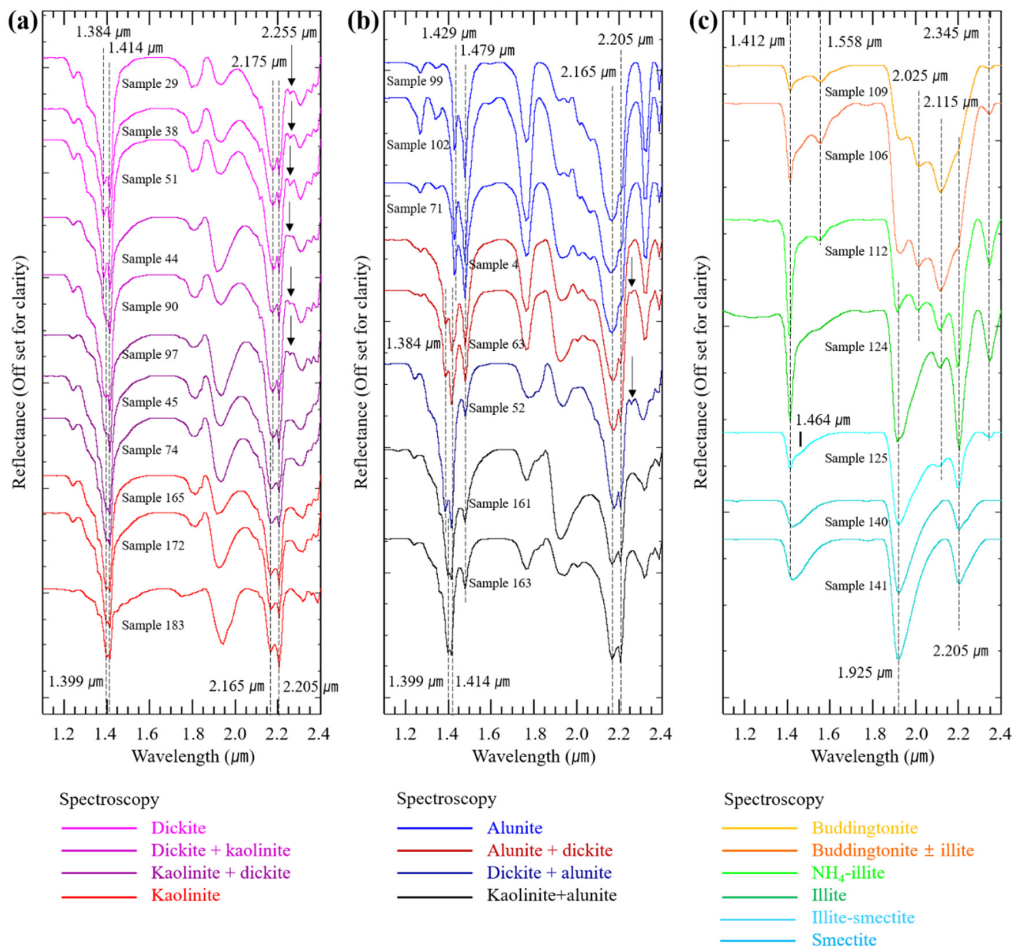


**Figure 5.** Representative reflectance spectra of samples collected from the acid alteration rock surface of the prospects. (a) Spectra of kaolin group minerals; (b) spectra of alunite and alunite + kaolin group minerals; (c) spectra of illite/smectite and ammonium minerals.

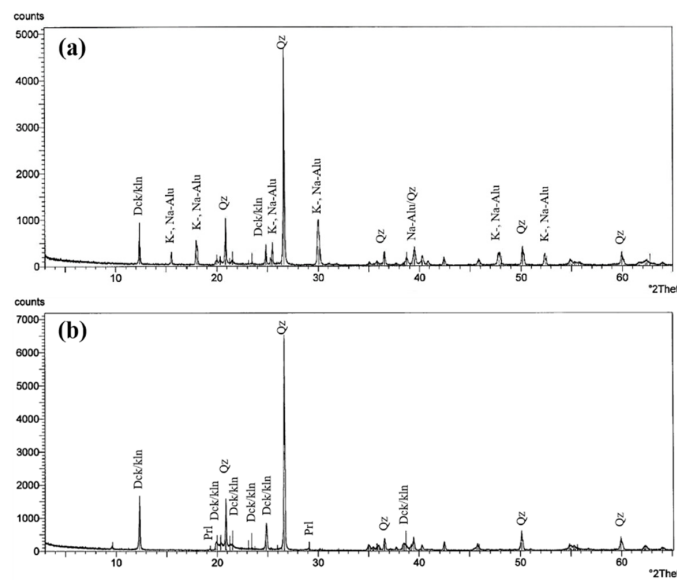


**Figure 6.** XRD spectrum of (a) sample TS107 in Figure 3c and (b) sample TS138 in Figure 3i. Abbreviations: alu = alunite, dck = dickite, kln = kaolinite, prl = pyrophyllite, and qz = quartz.

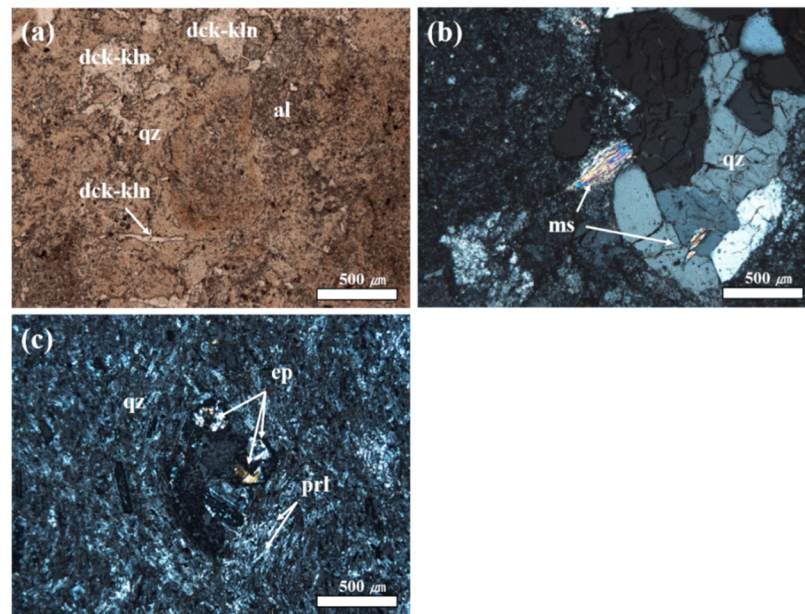


**Figure 7.** Photomicrographs of altered rock samples in the eastern Tsogttsetsii prospects: (a) transmitted light photomicrograph (uncrossed polarizers) of alunite mixed with dickite and kaolinite (sample TS107 in Figure 3c, Appendix A); (b) transmitted light photomicrograph (crossed polarizers) of muscovite with coarse quartz crystal (sample TS128A in Figure 3j, Appendix A); and (c) transmitted light photomicrograph (crossed polarizers) of pyrophyllite (sample TS138 in Figure 3i, Appendix A). Abbreviations: al = alunite, dck = dickite, ep = epidote, kln = kaolinite, ms = muscovite, prl = pyrophyllite, and qz = quartz.

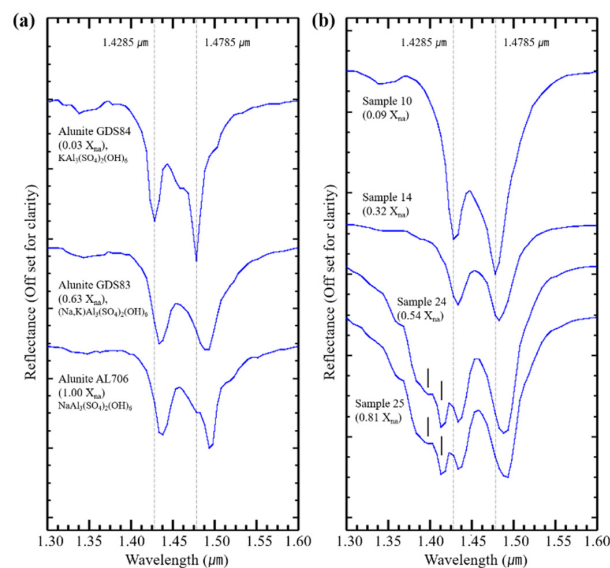


**Figure 8.** Reflectance spectra of alunite showing the OH overtone doublet absorptions shift at 1.429 and 1.479  $\mu\text{m}$  with K and Na components.  $X_{\text{Na}}$  is the mole fraction of Na in the alunite. As the Na content increases, the OH overtone doublet absorption in the spectrum of K-alunite shifts to longer wavelengths. (a) Representative United States Geological Survey (USGS) reflectance spectra of well-characterized alunite [35] and (b) field reflectance spectra for alunite collected from the rock surface of eastern Tsogttsetsii.  $X_{\text{Na}}$  was calculated using the wavelength correlation method of [29]. The accuracy of this method using the absorption peak near 1.479  $\mu\text{m}$  was  $\pm 0.05 X_{\text{Na}}$  at a spectral resolution of 1 nm and  $\pm 0.1 X_{\text{Na}}$  at a spectral resolution of 10 nm.

When classified based on  $X_{Na}$ , 59% of all alunite samples were K-rich ( $X_{Na} < 0.2$ ) (e.g., sample 10, Figure 8b), 32% had an intermediate composition ( $0.2 < X_{Na} < 0.8$ ) (e.g., samples 14 and 24, Figure 8b), and 9% were Na-rich ( $X_{Na} > 0.8$ ) (e.g., sample 25, Figure 8b). Na-rich alunite was only found in Prospect I (Table A1). Although four alunite spectral samples were identified to have a high Na composition (samples 16, 25, 26, and 27, Table A1), their rock samples were not collected during the field investigation. The  $X_{Na}$  of the spectrum (sample 36, Table A1) collected at the same location as the rock sample TS104 (Figure 3a; Table A1) was 0.32, indicating that it is a K-Na alunite with an intermediate composition. This was confirmed by an EPMA analysis with thin sections. Electron microprobe elemental maps of the rock sample TS104 show alunite crystal compositional zoning with K-rich cores surrounded by a K and Na-bearing alunite rim (Figure 9a,b). In contrast, the electron microprobe elemental map of the rock sample TS140A with low  $X_{Na}$  (0.09) was mostly filled with K components (Figure 9c,d). Almost all alunite spectrum samples identified in Prospects II and III indicate K-rich alunite (Table A1).

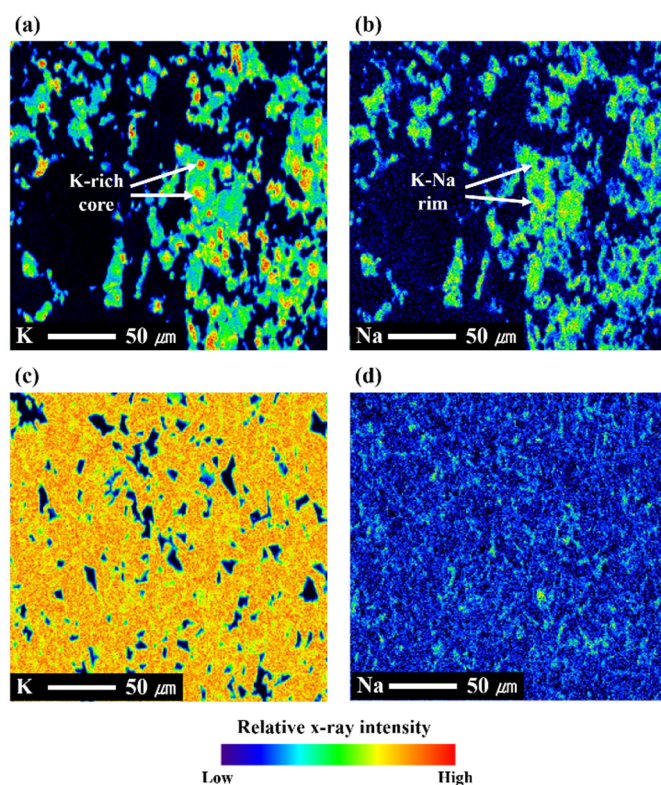


**Figure 9.** Electron microprobe elemental maps for samples collected from the alunite zones of Prospect I. Color bar shows relative X-ray count levels for elements. (a) K element map of rock sample TS104; (b) Na element map of rock sample TS104; (c) K element map of rock sample TS40A; (d) Na element map of rock sample TS40A.

An examination of the field spectra indicates kaolinite, dickite, and their mixtures, which are common minerals for advanced argillic alteration assemblage [2]. Dickite [ $Al_2Si_2O_5(OH)_4$ ] spectra possess an intense doublet combination Al-OH absorption feature at 2.175 and 2.205  $\mu m$ , and a doublet OH overtone feature at 1.384 and 1.414  $\mu m$  (Figure 5a). Some of the sample spectra exhibited a doublet combination OH feature at 2.165 and 2.205  $\mu m$  and a doublet OH overtone feature near 1.399 and 1.414  $\mu m$ , which are typical of kaolinite [ $Al_2Si_2O_5(OH)_4$ ] (Figure 5a). Some samples show a mixture of dickite and kaolinite (Figure 5a). The degree of crystallographic disorder may significantly impact the shape of the spectral features in kaolinite [4]. Figure 10 shows a variation of the shape of the doublet combination OH feature at 2.165 and 2.205  $\mu m$  from well crystallized (WXL) kaolinite to poor crystallized (PXL) kaolinite. Field spectral analysis based on the doublet

combination OH feature indicates that WXL kaolinite is dominant in Prospect III (Table A1). Field spectra and XRD analysis indicate that dickite ± kaolinite was more abundant in Prospects I and II while kaolinite was more abundant in Prospect III.

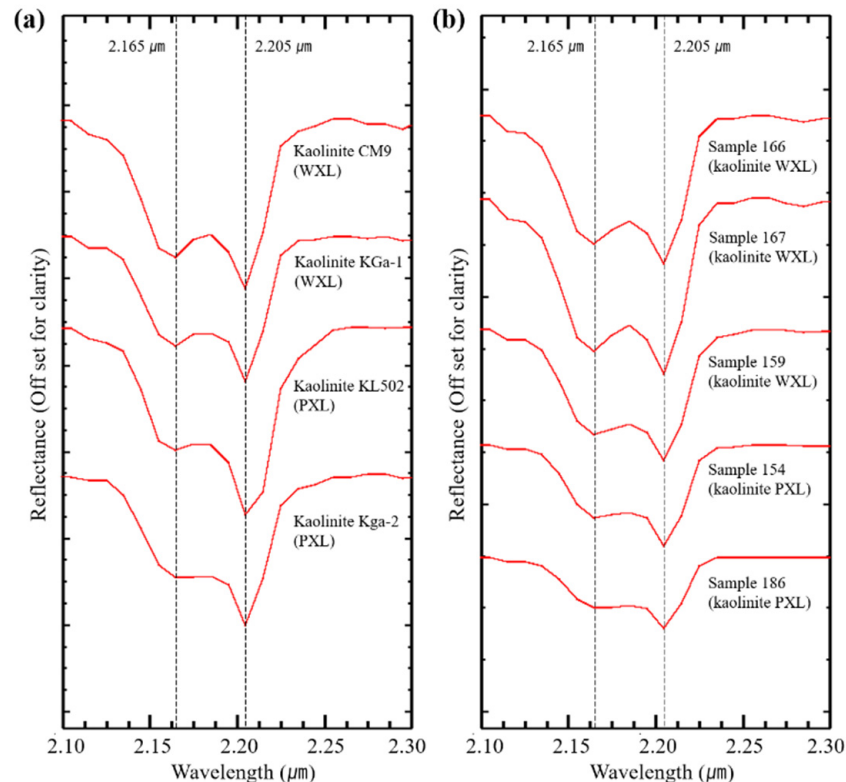


**Figure 10.** (a) Representative USGS reflectance spectra of kaolinite showing shape variations of the OH doublet combination at 2.165 and 2.205 μm from well crystallized (WXL) kaolinite to poorly crystallized (PXL) kaolinite [35]; (b) kaolinite spectra collected from the rock surface of Prospect III, showing variation of crystalline.

The illite  $[(K,H_3O)(Al,Mg,Fe)_2(Si,Al)_4O_{10}[(OH)_2,H_2O]]$ , smectite  $[(Na,Ca)_{0.33}(Al,Mg)_2(Si_4O_{10})(OH)_2 \cdot nH_2O]$ , and mixed-layered illite-smectite (Figure 5c) commonly occurring in low-intermediate sulfidation epithermal deposits [56] were identified mainly in Prospects I and II (Table A1). These minerals share absorption features near 1.412 (OH, H<sub>2</sub>O), 1.925 (H<sub>2</sub>O), and 2.205 μm (Al-OH), with spectroscopic differences (Figure 5c). Illite has an absorption feature at 2.345 μm and a deeper Al-OH absorption feature at 2.205 μm than for the H<sub>2</sub>O absorption feature at 1.925 μm. In contrast, smectite exhibits a shallow Al-OH absorption and much deeper H<sub>2</sub>O absorption. The mixed-layered illite-smectite shows an intermediate spectrum between illite and smectite. The H<sub>2</sub>O/Al-OH depth ratio proposed by [40] was used to distinguish illite, smectite, and mixed-layered illite-smectite (>0.96 illite, 0.76 < illite-smectite < 0.96, and < 0.76 smectite) (Figure 11). Based on the H<sub>2</sub>O/Al-OH depth ratio, the mixed-layered illite-smectite spectra were identified mainly in samples of Prospects I and II, and a few spectra of illite and smectite were also identified in all prospects (Table A1). Previous studies have demonstrated a strong correlation between the abundance of Al in the octahedral layer (Al<sup>oct</sup>) of the illite/muscovite compositional series and the wavelength position of the 2.2 μm absorption feature [29]:

$$Al^{oct} = (\lambda - 2.293) / -0.05226 \quad (2.194 < \lambda < 2.217 \text{ } \mu\text{m}) \quad (3)$$

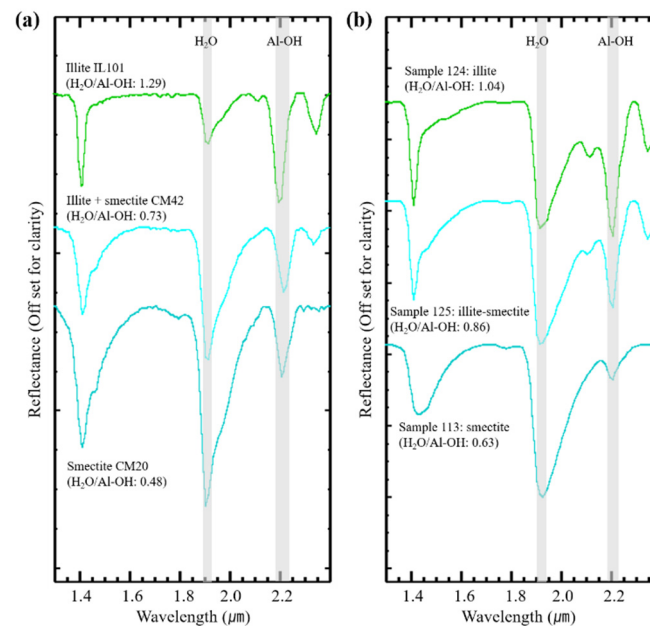


**Figure 11.** (a) Representative USGS reflectance spectra of illite, mixed-layered illite-smectite, and smectite with calculated  $H_2O/Al-OH$  depth ratios [35]; (b) representative field reflectance spectra of illite, mixed-layered illite-smectite, and smectite with calculated  $H_2O/Al-OH$  depth ratios.

As  $Al^{oct}$  decreases due to the substitution of Mg and/or Fe in the octahedral site, the 2.2  $\mu m$  absorption shifts to longer wavelengths. The spectra of the illite/muscovite compositional series identified in Prospects I and II exhibited wavelength positions for Al-OH absorption between 2.195 and 2.215  $\mu m$  (Figure 11). Based on the  $Al^{oct}$  content of the illite/muscovite compositional series according to the wavelength position of [29], high Al illite/muscovite compositional samples were identified in Prospect I ( $Al^{oct} = 1.875$ , samples 107 and 110 in Table A1), and it was confirmed that there was low Al illite/muscovite in Prospect II ( $Al^{oct} = 1.684$ , e.g., samples 138 and 142 in Table A1). The  $Al^{oct}$  content of low illite/muscovite compositional samples based on microprobe measurements of three to five mineral grains in each sample were similar to the  $Al^{oct}$  content based on spectroscopy (TS108A and TS128A, Table A1; Figure 7b). A laboratory analysis for high Al composition was not conducted because rock samples were not collected at the location of the spectral measurement.

Although buddingtonite and  $NH_4$ -illite are generally not associated with advanced argillic alteration, they may be formed in both hydrothermal and sedimentary environments [57], and are common in low-sulfidation epithermal environments [36]. The spectral absorption features exhibited by some samples in Prospect I indicate the presence of buddingtonite [ $NH_4AlSi_3O_8$ ], an ammonium feldspar, which has its primary  $NH_4$  absorption features at 2.025 and 2.115  $\mu m$ , and the secondary feature at 1.558  $\mu m$  (Figure 5c). Spectrum 112 (Figure 5c) collected in Prospect I, with  $NH_4$  and Al-OH absorption features at 2.205  $\mu m$ , indicates the presence of  $NH_4$  illite [ $(NH_4,K)Al_2(Si_3Al)O_{10}(OH)_2$ ].

The resampled WV-3 SWIR field spectra revealed the absorption features of hydrothermal alteration minerals, even with the limited SWIR spectral resolution (Figure 4). Kaolinite and dickite were difficult to distinguish with the WV-3 SWIR resolution (Figure 4c,d), and therefore, these minerals were grouped in the kaolin spectral category. The alunite and kaolin group mineral spectra were similar in shape; however, the strongest Al-OH absorption feature was located at 2.163  $\mu m$  (band 5) in alunite and at 2.202  $\mu m$  (band 6) in kaolin group minerals (Figure 4a,c,d). Mixed spectra of the alunite and kaolin group minerals were distinguishable from the alunite and kaolin group mineral spectra because they approximately have the same reflectance in the WV-3 SWIR bands 5 and 6 (Figure 4b). The resampled WV-3 buddingtonite and  $NH_4$ -illite spectra showed spectral absorption

features at SWIR bands 2 and 5 due to the presence of  $\text{NH}_4$ , and at SWIR band 6 due to Al-OH (Figure 4e,f). Despite the similar spectral features of buddingtonite and  $\text{NH}_4$ -illite, the difference for maximum absorption in bands 5 and 6, respectively, allows them to be distinguished. The resampled WV-3 field spectra of illite and mixed layered illite-smectite show similar strong absorption features in WV-3 SWIR band 2 (from OH and  $\text{H}_2\text{O}$ ) and band 6 (from Al-OH) (Figure 4g,h). As with dickite and kaolinite, the spectra of illite and mixed layered illite-smectite were very similar in the WV-3 SWIR spectral resolution, and as such, we defined them as illite/smectite in this study. In contrast, the resampled WV-3 field spectrum of smectite exhibited a weak absorption feature for Al-OH in the WV-3 SWIR band 6 (Figure 4i).

#### 4.2. Decorrelation Stretch and Band Math Analysis

The most useful WV-3 SWIR band combination of DS for the study area consists of SWIR band 2 (1.570  $\mu\text{m}$ ) in red, band 5 (2.165  $\mu\text{m}$ ) in green, and band 6 (2.205  $\mu\text{m}$ ) in blue, highlighting the spectral properties of rocks related to bulk mineralogical differences (Figure 12a). According to the additive color synthesis, red in this DS image means high reflectance in band 2, and low reflectance in bands 5 and 6, linked to the spectral absorption features of advanced argillic minerals such as alunite and kaolin group minerals (Figure 4a–d). The relatively high reflectance in bands 2 and 6 and low reflectance in band 5 creates a pink color in this image, closely related to the reflecting spectral absorption feature of buddingtonite (Figure 4e). Yellow appears because of high reflectance in bands 2 and 5, and the reflectance in band 6, corresponding to the spectral characteristic of illite/smectite and smectite (Figure 4g–i). Red, pink, and yellow regions correspond to the prospects in the Permian subvolcanic rocks where field verification and rock sample analysis showed the development of hydrothermal alteration (Figures 1 and 3). The DS image also shows a wide yellow region in the northern part of the image, suggesting the presence of illite/smectite or smectite. The blue color to the south of the DS image depicts volcanogenic sedimentary rocks developed in the northeast–southwest direction.

Advanced argillic minerals such as alunite and the kaolin group possess Al-OH spectral absorption features at 2.165–2.175  $\mu\text{m}$  and 2.205  $\mu\text{m}$ , corresponding to WV-3 SWIR bands 5 and 6, respectively (Figure 4a–d). A BM, SWIR band 2  $\times$  SWIR band 7/SWIR band 5  $\times$  SWIR band 6 (threshold values  $> 1.1$ ), was used to map advanced argillic alteration by highlighting the Al-OH spectral absorption feature. Brighter pixels in the BM image were closer to the Al-OH spectral absorption property of advanced argillic minerals (Figure 12b). The Al-OH spectral absorption was strong and wide in Prospects I and III and weak in Prospect II. Field reflectance measurements show that the BM also mapped ammonium mineral (buddingtonite and  $\text{NH}_4$ -illite)-rich rocks (Figure 12b) due to an overlap of the Al-OH and the  $\text{NH}_4$  spectral absorption features at WV-3 SWIR bands 5 and 6 (Figure 4e,f).

Field spectra from the prospects shows that the illite/smectite and smectite SWIR spectral absorption features due to OH,  $\text{H}_2\text{O}$ , and Al-OH at 1,412, 1,464, and 2,205  $\mu\text{m}$ , respectively (Figure 5c), were defined by WV-3 SWIR bands 2 and 6 (Figure 4f). The SWIR band 5 reflectance of illite/smectite and smectite was higher than that of other Al-OH absorption minerals such as the alunite and kaolin group. Therefore, to map illite/smectite and smectite, a BM SWIR band 5  $\times$  SWIR band 7/SWIR band 6  $\times$  SWIR band 6 ( $> 1.07$ ) was used. The Al-OH spectral absorption of illite/smectite and smectite was observed in all prospects (Figure 12c), in particular, the broadly bleached zones of Prospects I and II (Figure 3j). The BM also mapped Al-OH spectral absorption of illite/smectite and smectite in the northern part of the study area. A field investigation indicated that the BM maps some alunite and kaolin group mineral-rich rocks (Figure 12c) because of the strong Al-OH absorption for this group in WV-3 SWIR band 6 (Figure 4c,d).

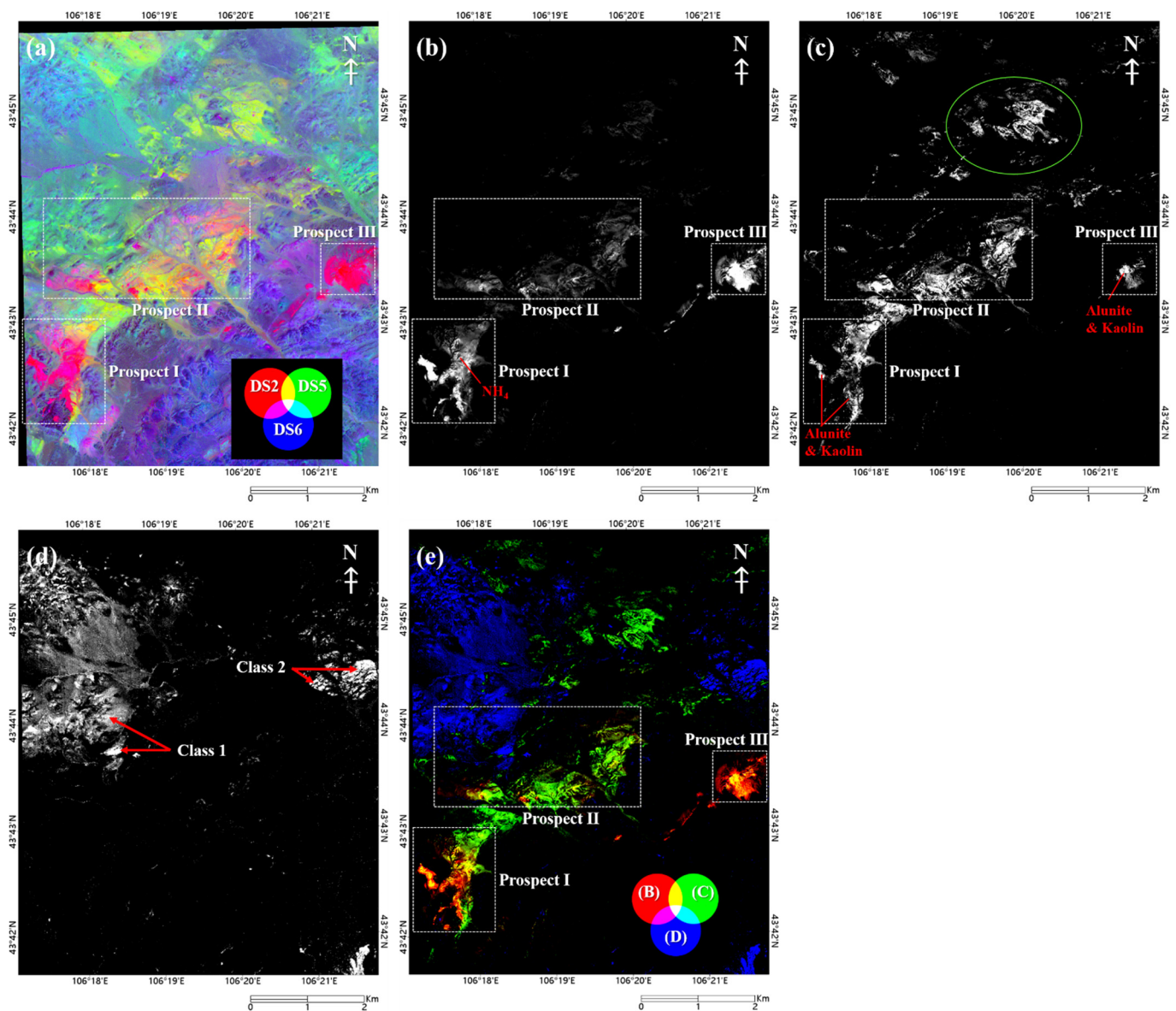


**Figure 12.** (a) WV-3 DS image of the eastern Tsogttsetsii (SWIR band 2 = red, SWIR band 5 = green, SWIR band 6 = blue); (b)–(d) WV-3 BM images of the eastern Tsogttsetsii: (b) advanced argillic alteration ( $\text{SWIR band 2} \times \text{SWIR band 7} / \text{SWIR band 5} \times \text{SWIR band 6} > 1.1$ ); (c) illite/smectite alteration ( $\text{SWIR band 5} \times \text{SWIR band 7} / \text{SWIR band 6} \times \text{SWIR band 6} > 1.07$ ); (d) chlorite ( $\text{SWIR band 6} / \text{SWIR band 8} > 1.03$ ); and (e) a false color composite image (red = advanced argillic alteration, green = illite/smectite alteration, blue = chlorite).

The Fe and Mg-OH absorption minerals, such as epidote and chlorite, and  $\text{CO}_3$  absorption minerals, such as calcite and dolomite, have their main spectral absorption features situated approximately in the 2.315, 2.325, and 2.335  $\mu\text{m}$  regions, corresponding to the WV-3 SWIR band 8 (Figure 13). The WV-3 band ratio of SWIR band 6/SWIR band 8 as suggested by [22] was used to map rocks with strong Fe, Mg-OH, and  $\text{CO}_3$  spectral absorption features. The band ratio of SWIR band 6/SWIR band 8 ( $> 1.03$ ) shows that Fe, Mg-OH, or  $\text{CO}_3$ -rich units occur widely in the northwestern and partially northeastern parts of the study area. There were no field spectra for these areas because field investigation focused on the prospects of the Permian subvolcanic rocks. Therefore, we compared average image spectra of regions extracted by the band ratio SWIR band 6/SWIR band 8 with the spectra of the USGS spectral library (Class 1 and Class 2 in Figures 12d and 13). The comparison with the WV-3 resampled USGS spectra in Figure 4 shows that the overall SWIR shape of the average image spectra was similar to the chlorite spectrum, with a

strong Fe, Mg-OH absorption feature at SWIR band 8 (2.329  $\mu\text{m}$ ). The average image spectra also appeared to be similar to the  $\text{CO}_3$  absorption of dolomite; however, the slope between bands 5 and 1 was closer to that of chlorite.

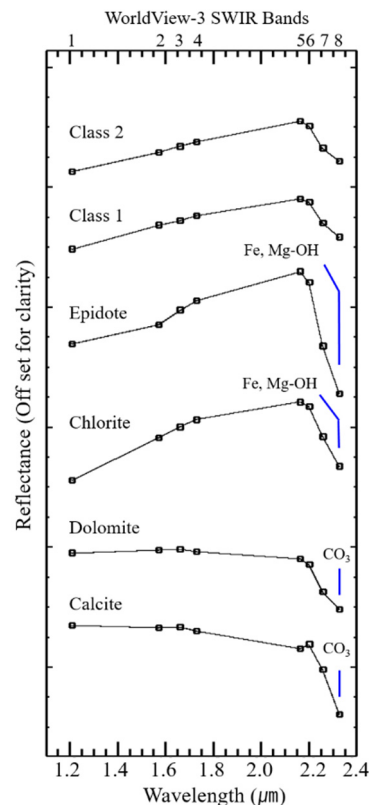


**Figure 13.** Comparison of WV-3 image spectra (class 1 and class 2) with USGS spectra (epidote, chlorite, dolomite, and calcite; [35]). WV-3 image spectra are the average for pixels from the SWIR band 6/SWIR band 8 BM image in Figure 7d. USGS spectra were resampled to WV-3 SWIR wavelength ranges.

Figure 12e presents a color composite image with SWIR band 2  $\times$  SWIR band 7/SWIR band 5  $\times$  SWIR band 6 in red, SWIR band 5  $\times$  SWIR band 7/SWIR band 6  $\times$  SWIR band 6 in green, and SWIR band 6/SWIR band 8 in blue. The red to yellow colors represent advanced argillic alteration including the alunite and kaolin group minerals, and ammonium minerals including buddingtonite and  $\text{NH}_4$ -illite in the Permian subvolcanic rocks (noticeable in Prospects I and III). The green colors characterize illite/smectite and smectite alterations in the Permian subvolcanic and bleached rocks (noticeable in Prospect II). The blue colors represent Fe and Mg-OH-rich rocks.

#### 4.3. Mixture-Tuned-Matched Filter Mineral Map

The mean WV-3 SWIR spectra in the same area as the known minerals identified by field spectral measurements, DS, and band ratio images (Figures 4 and 12) were used as endmembers in MTMF mineral mapping (Figure 14). The WV-3 MTMF mineral map was produced for the surface of the study area (Figure 15). Pixels corresponding to a high MF score and low infeasibility for each mineral class were assigned a color. Within one pixel of the WV-3 SWIR image, alteration minerals were mixed in various proportions, while each pixel could be assigned to eight mineral spectra representing spectral and spatially dominant phases. The MTMF mapping results clearly explain the hydrothermal alteration mineralogy of the study area more so than the results derived from an analysis of the DS and band ratios. This is done by illustrating the spatial distribution of individual alteration minerals (Figures 12 and 15).

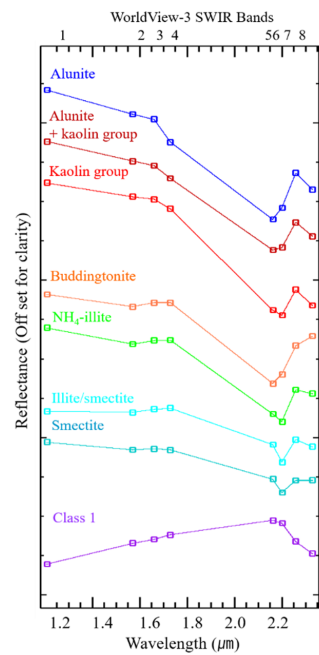


**Figure 14.** WV-3 SWIR endmember spectra for mixture-tuned-matched filter mineral mapping of the study area. Each endmember spectrum is an average of spectra from nine adjoining pixels from the same area as the known minerals identified by the field spectral measurements, DS, and band ratio images.

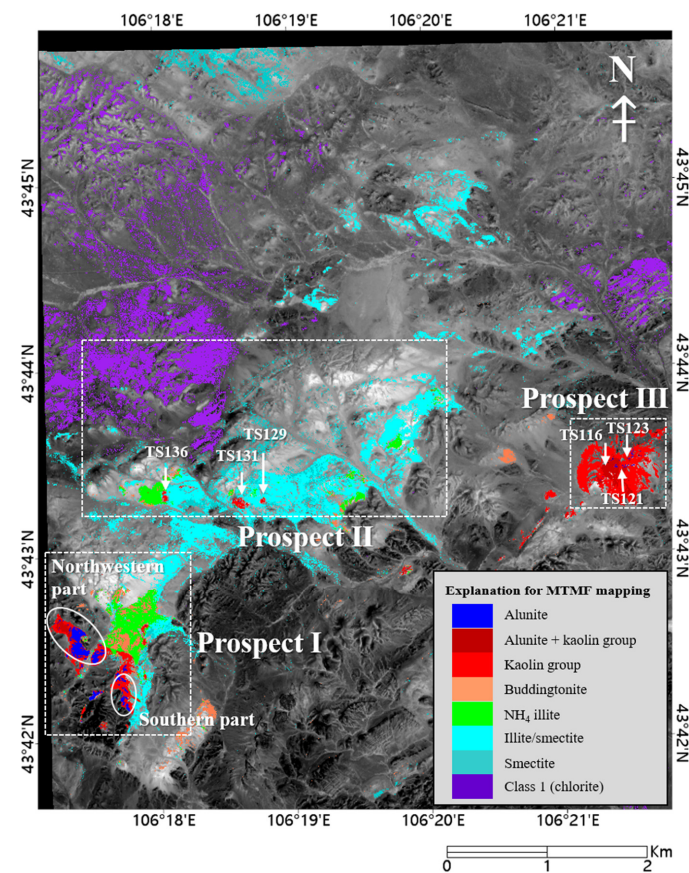


**Figure 15.** Mixture-tuned-matched filter (MTMF) mineral map showing spectrally predominant minerals at the study area using WV-3 SWIR. Each mineral class was overlaid on the WV-3 SWIR band 1 image.

The most prominent feature on the MTMF map is the presence of kaolin group mineral zones in all prospects and alunite in the center of these zones, independent of scale (Figure 15). Prospect 1 contains two elliptical zones of kaolin group minerals, each trending in the NS and NW directions. In Prospect II, three small circular zones of kaolin group minerals were observed, and a circular zone of kaolin group mineral with an approximate radius of 500 m is present in Prospect III. The MTMF mineral map confirms buddingtonite,  $\text{NH}_4$ -illite distribution in Prospects I and II. Unlike Prospects I and II, there was an absence of large areas of ammonium minerals and illite/smectite in Prospect III, whilst smectite was detected.

Prospect I: Alunite, kaolin group minerals, buddingtonite,  $\text{NH}_4$ -illite, illite/smectite, and smectite were mapped at Prospect I (Figure 15). Alunite, surrounded by kaolin group minerals, was mapped in large outcrops in the southern and northwestern parts of Prospect I, matching the field survey (Figure 3a–i; TS113, TS140 in Figure 16b; Table A1). In particular, in the south of the northwestern outcrop hill, the alunite was mapped widely in the study area, and the alunite + kaolin group minerals predominates northward (Figure 16b). The 3D side view of the northwestern outcrop hill, overlaid on the DEM, shows that the alunite ± kaolin group in the upper part and the kaolin group in the lower part was laterally well developed (Figure 17). The lateral development of advanced argillic alteration was consistent with field observations (Figure 3a–i). The MTMF map shows an abrupt transition from kaolin group minerals to ammonium minerals, buddingtonite, and  $\text{NH}_4$ -illite, at the north of the southern outcrop (black dashed line in Figure 16b). These ammonium minerals are widely distributed in the northeast. Illite/smectite and smectite was observed along the drainage from south to northeast in Prospect I (Figures 15 and 16).

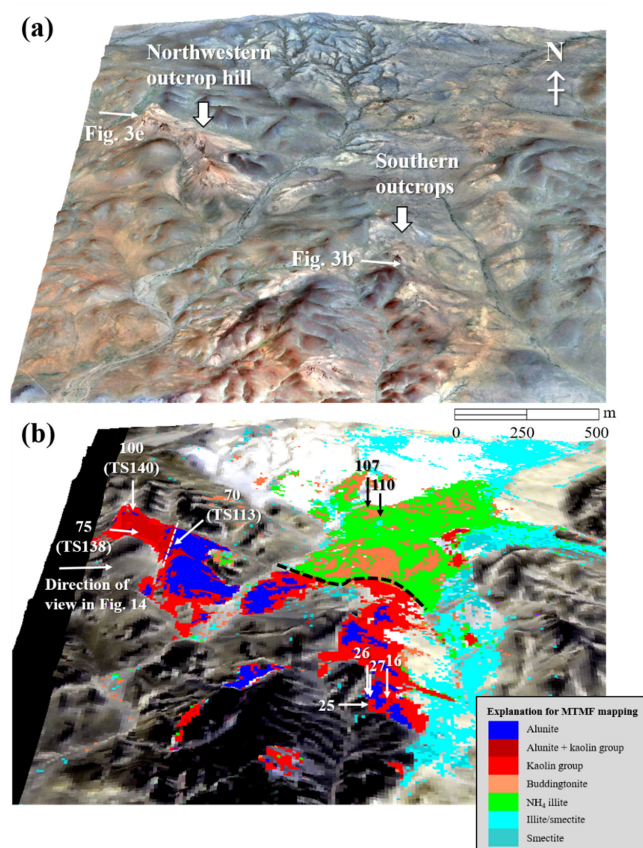


**Figure 16.** (a) 3D view of the orthophotograph overlaid on the digital elevation model (DEM) generated by drone photogrammetric methods at Prospect I. The vertical exaggeration is 3×. (b) 3D view of the MTMF mineral map overlaid on the drone-based DEM generated by the drone photogrammetric method at Prospect I. The vertical exaggeration is 3×. The scale bar is approximate.

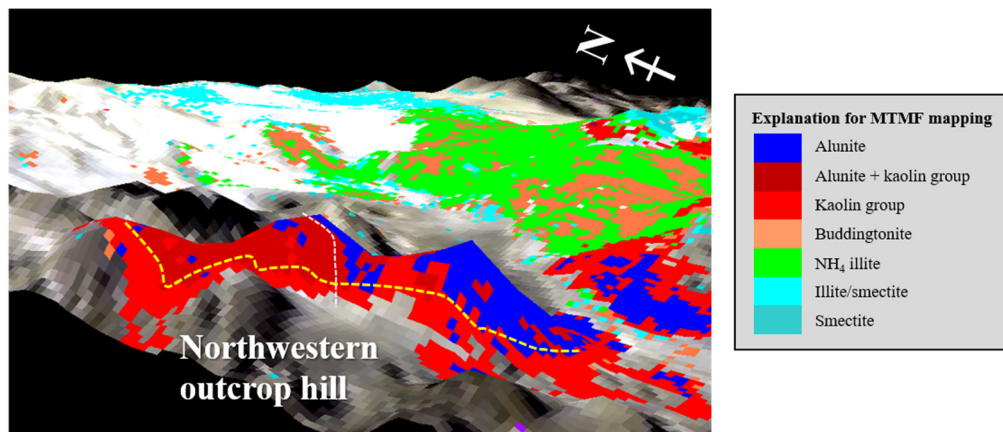


**Figure 17.** 3D side view of the MTMF mineral map overlaid on the DEM generated by the drone photogrammetric method at the northwestern outcrop hill. The vertical exaggeration is 3×.

Prospect II: The MTMF map shows extensive areas of illite/smectite and smectite extending from the south to southeast along a fault (Figures 1b and 15). These areas are consistent with bleached zones. Small areas of kaolin group minerals, with minor alunite and alunite + kaolin group were observed in the south central and southwest parts of Prospect II (Figure 15), consistent with field verification (Figure 3j–o; TS129, TS131, TS136 in Figure 15; Table A1). Although there were no field spectral measurements for buddingtonite and NH<sub>4</sub>-illite in Prospect II, ammonium minerals were identified from the MTMF map. Although small in size, the ammonium minerals, as per Prospect I, appeared as a transition zone along with the southwestern kaolin group minerals (location near TS136 in Figure 15). Buddingtonite and NH<sub>4</sub>-illite were also detected along the eastern illite/smectite alteration zone of Prospect II. Chlorite was extensively present in the northwestern part of Prospect II that corresponds to volcanic and sedimentary rocks (Figure 1).

Prospect III: this prospect has a zone with alunite + kaolin group minerals surrounded by kaolinite (Figure 15), consistent with field verification (Figure 3p,q; TS116, TS121, and TS123 in Figure 15; Table A1). Although alunite was found in Prospect III, compared to Prospect I, it consisted of a very small area of a few pixels.

#### 4.4. Accuracy Assessment of MTMF Mapping

Table 2 shows the confusion matrix for evaluating the accuracy of the MTMF mineral mapping and the performance of the WV-3 SWIR bands. There were 190 field spectral measurements excluding two samples with uncertain mineral determination. These measurements were divided into seven mineral classes for comparison with the MTMF mapping results (Table 2). The overall accuracy was 65.8% and the kappa index was 0.473. The user accuracy of alunite was 75.6%. The alunite + kaolin group had high errors with the kaolin group class (commission: 67.7%, omission: 45.5%). The high commission error with this class means that the kaolin group minerals have been incorrectly mapped as the alunite + kaolin group. This commission error may be related to the difference in spatial resolution between the field spectral measurements and the WV-3 SWIR data. Field spectral measurements are signals recorded from the surface of a few centimeters of rock, while the WV-3 SWIR pixel spectrum represents 7.5 m of space. At certain locations, the field spectral measurement was kaolinite, although alunite may also be included in a 7.5 m pixel. The high omission error of the alunite + kaolin group indicates that the presence of this mixture is more extensive than that in the MTMF map. This omission error may be related to the spectral resolution of the WV-3 SWIR data, which indicates that there are limitations in distinguishing small spectral feature differences (the alunite + kaolin group spectrum is very similar to the kaolin group and alunite spectrum, see Figure 14). The confusion matrix shows that the kaolin group was the best mapped with user accuracy

of 85.9% Omission errors for buddingtonite and  $\text{NH}_4$ -illite were lacking, although they had commission errors with the illite/smectite (50%) and smectite classes (50%). There were only four references for ammonium minerals, which made it difficult to evaluate their accuracy. Similar to the case of the alunite + kaolin group, illite/smectite was highly confused with smectite (30.8%). Smectite had the lowest producer and user accuracy, at 16.7% and 20%, respectively. This may be because the spectral absorption of smectite is so weak that it can easily be obscured by other mineral spectral absorptions.

**Table 2.** Confusion matrix comparing field spectral measurements to MTMF mapping result. Overall accuracy = 65.8% (125/190) and kappa = 0.473.

		Reference Data (Field Spectral Measurements)						Row Total (User Accuracy, %)
		Alunite	Alunite + Kaolin Group	Kaolin Group	Buddingtonite NH <sub>4</sub> -Illite	Illite/Smectite	Smectite	
MTMF Class	Alunite	32	1	8	0	0	0	41 (75.6)
	Alunite + Kaolin group	7	3	21	0	0	0	31 (12.9)
	Kaolin group	6	5	79	0	0	1	92 (85.9)
	Buddingtonite	0	0	0	3	0	1	2 (50)
	NH <sub>4</sub> -Illite	0	0	0	0	1	0	1 (50)
	Illite/smectite	0	0	2	0	0	6	8 (66.7)
	Smectite	0	0	0	0	0	4	4 (20)
	Unclass	0	0	3	0	0	1	4
	Column total (producer accuracy, %)	45 (72.1)	9 (36.4)	113 (69.9)	3 (100)	1 (100)	13 (46.2)	6 (16.7)

## 5. Discussion

The field spectroscopy and WV-3 MTMF mineral mapping results indicate the complex distribution of various alteration mineral assemblages in the eastern Tsogttsetsii district. The results of mineral mapping alone do not constrain the hydrothermal processes, and further investigation and experimentation are necessary to understand the process of alteration in the region. The WV-3 SWIR data and field spectral measurements provide complementary information needed to interpret hydrothermal processes in the study area, and suggest some locations for further mineral exploration.

The SWIR spectra of alunite at Prospect I had various compositions of K and Na-containing alunite endmembers and components between them (Table A1). Previous studies [1,58,59] suggest that the substitution of K by Na in alunite was favored at higher temperatures given a similar host rock type and was spatially and genetically associated with ores. Chang et al. [6] found that as they approached the intrusive center of the Lepanto porphyry Cu lithocap, the alunite absorption peak near 1480 nm shifted to higher wavelengths due to the higher Na and lower K content in the alunite. High Na-endmember composition ( $X_{\text{Na}} = 0.81$ ) was found in the SWIR spectra of alunite south of the southern outcrop in Prospect I (samples 16, 25, 26, and 27 in Figure 16b; Table A1). There are no rock samples for Na alunite, and therefore, further investigation (rock sampling and chemical analysis) in the southern outcrop is required to confirm the results of the spectral data analysis.

The SWIR spectra of dickite, commonly present in high sulfidation systems, were abundant in Prospects I and II (Table A1), indicating a relatively deep erosion exposure of the hydrothermal system. The joint detection of dickite, pyrophyllite, and Na alunite may be a clue to the intrusive center of the high sulfidation system (e.g., [2,6]). The presence of dickite, pyrophyllite and Na-alunite was verified by XRD and EPMA analyses of a sample collected from the northwestern hill of Prospect I (TS 138 in Figures 6b and 7c; Table A1),

but the small amount of pyrophyllite and Na-alunite, means that it was spectroscopically dominated by dickite. Further investigation of the area around the sample collection location is required.

Kaolinite was relatively less abundant in Prospects I and II than in Prospect III, due to the higher occurrence of alunite and dickite. The SWIR spectra of kaolinites at Prospects was mainly for high crystalline varieties (Table A1). WXL kaolinites are observed in acidic hydrothermal systems or in weathering environments [4,60]. At Prospects, co-occurrence with high temperature alteration minerals (dickite, alunite, and pyrophyllite) suggests that WXL kaolinites were formed by hydrothermal activity.

Lithocaps form when acidic magmatic-hydrothermal fluids, ascending towards the paleosurface or along permeable structures react with wall rocks. They are composed of rocks that have silicic, advanced argillic and argillic alteration assemblages with laterally extensive alteration zones greater than 10 km for example in Yanacocha, Peru, and Shuteen, Mongolia [32,61]. Most observed lithocaps are only erosional remnants, which may either wholly or partially overlie and conceal high sulfidation porphyry-style mineralization and can cover intermediate sulfidation epithermal veins (e.g., [1,2,6]). At the surface of the eastern Tsogttsetsii prospects, the laterally well-developed advanced argillic alteration, including abundant dickite, kaolinite, K-alunite, Na-alunite, silicification, and vuggy quartz, showed similar characteristics to lithocaps that host high-sulfidation systems. Cuprite, Nevada possesses advanced argillic alteration assemblages present in many ore deposits. Many points of evidence, for example the lack of abundant pyrite, and recognition of a steam-heated alunite stable isotope signature, suggest the presence of a low sulfidation hydrothermal system where no significant precious metal mineralization has been recognized [33]. More work, such as isotopic dating, stable isotope analysis, and geophysical surveys, is necessary to understand the detailed stages and zonation of hydrothermal alteration by fluid migration in the eastern Tsogttsetsii prospects.

In the northern area of the southern outcrop of Prospect I, spectroscopically high  $Al^{oct}$  illite-smectite spectra was identified (samples 107 and 110, Table A1), potentially relating to the leaching of Mg and/or Fe by hydrothermal fluids (similar to muscovite) [62]. Although the WV-3 spectral resolution makes it difficult to classify the grade of Al composition, the MTMF map confirms the distribution of the illite/smectite at locations where high  $Al^{oct}$  illite-smectite was identified (sample 110 in Figure 16b). There were only two field spectral measurements, however, and there were no rock samples available for laboratory analysis. The correlation between the absorption wavelength position of the illite-smectite and its  $Al^{oct}$  composition could not be verified. Most illite compositional samples identified in Prospect II were of a low Al composition with a wavelength longer than 2.2  $\mu m$  (Figure 5, Table A1). Low  $Al^{oct}$  illite compositional spectra may be associated with highly permeable lithologies and low temperature and/or acidity environments [36].

When K is replaced by ammonium ( $NH_4$ ) in illite, smectite, mixed-layered illite-smectite, muscovite, alunite, jarosite, and adularia, it generates ammonium-bearing minerals [37]. Neither ammonium minerals (buddingtonite and  $NH_4$  illite) nor ammonium-bearing rocks have visible diagnostic properties and the XRD pattern of buddingtonite can be easily mistaken for the K-feldspar pattern [35]. Due to the distinct spectral properties, they have been identified using SWIR spectroscopy in some hydrothermal ore deposits (e.g., [37,63]). In our field SWIR spectroscopy, only four samples were identified as ammonium minerals (samples 106, 107, 109, and 112, Table A1), but the MTMF map shows the wide distribution of ammonium minerals in the northeast part of the southern outcrop in Prospect I and in some parts in Prospect II (Figure 15), potentially expanding spatially limited fieldwork results. The wide distribution of ammonium minerals may be associated with low-sulfidation adularia-sericite-type alteration [64].

## 6. Conclusions

The WV-3 SWIR data are effective for mapping alteration minerals in areas where access is limited. Its complementary use with field SWIR spectroscopy and other field

methods help to focus efforts on the ground. Combining WV-3 SWIR data and field SWIR spectroscopy with conventional exploration methods in unknown areas can narrow the selection between deposit models and facilitate mineral exploration.

Using DS, BM, and MTMF for WV-3 SWIR data, this study was able to map alteration minerals for the eastern Tsogttsetsii district. Three alteration categories including advanced argillic (alunite, dickite, and kaolinite), illite/smectite (illite, smectite, and mixed-layered illite-smectite), and ammonium minerals (buddingtonite and  $\text{NH}_4$ -illite) were mapped spectroscopically and verified by the laboratory analysis of field samples. Despite inherent limitations of the WV-3 SWIR data in terms of limited spectral resolution such as the inability to distinguish between kaolinite and dickite, and spatial resolution (7.5 m per pixel), the assessment of the WV-3 MTMF map using field SWIR data showed high accuracy of WV-3 SWIR data for minerals with distinct spectral characteristics such as alunite, the kaolin group, illite/smectite, buddingtonite, and  $\text{NH}_4$ -illite. However, the classification accuracy of mixed minerals (kaolin group + alunite) and weak spectral absorption mineral (smectite) was relatively low, which reduced the kappa coefficient and overall accuracy. The combination of WV-3 SWIR mineral mapping and drone photogrammetric-derived DEM contributed to understanding the structural development of the hydrothermal system by visualizing the topographic and spatial distribution of surface alteration minerals.

Field SWIR spectroscopy provides more detailed information for alteration minerals which cannot be determined with WV-3 SWIR data. The alunite contained K, Na, and mixed endmembers according to the absorption peaks. Dickite  $\pm$  kaolinite was found in Prospects I and II while WXL kaolinite was widely distributed in Prospect III. Most illite compositional samples had a low Al content with a longer wavelength from 2.2  $\mu\text{m}$ .

No evidence of metal mineralization was found at the surface of the eastern Tsogttsetsii district and nothing is known about what lies beneath the alteration zone. Not all alterations were related to ore bodies, and not all ore bodies were accompanied by alterations, however, the presence of major alterations on the surface was an indicator of possible deposits [10]. The prospects identified in this study were generally understood to be lithology-controlled alterations by lateral fluid flow. This may involve more distant alterations from the structure-controlled intrusive center. Therefore, it is recommended that future research focus on locating the center of the hydrothermal fluid by conducting vectoring by combining SWIR spectroscopy and whole rock geochemistry along the hydrothermal alteration zones identified in this study.

**Author Contributions:** Conceptualization, Y.-S.S.; methodology, Y.-S.S.; software, Y.-S.S. and E.-S.B.; validation, Y.-S.S.; formal analysis, Y.-S.S. and B.-W.Y.; investigation, Y.-S.S., B.-W.Y., E.-S.B., S.-J.C., H.-T.N., and H.B.; writing—original draft preparation, Y.-S.S. and E.-S.B.; writing—review and editing, Y.-S.S.; visualization, Y.-S.S., B.-W.Y., and H.B.; supervision, K.-E.K.; project administration, S.-J.C.; funding acquisition, S.-J.C. All authors have read and agreed to the published version of the manuscript.

**Funding:** This work was supported by the Korea Institute of Geoscience and Mineral Resources (KIGAM) Basic Research Project (21-3211) funded by the Ministry of Science and ICT of Korea. This work was also supported by a National Research Council of Science & Technology (NST) grant by the Korea government (MSIT) (No.CRC-15-06-KIGAM).

**Data Availability Statement:** Not Applicable.

**Acknowledgments:** We thank Eui-Jun Kim for help in the field observation and for comments that improved the manuscript.

**Conflicts of Interest:** The authors declare no conflict of interest.

## Appendix A

**Table A1.** Comparison of acid alteration mineralogy from field SWIR reflectance spectroscopy, WorldView-3 MTMF mapping, and XRD at the same locations.

Field Spectra Sample No. (Rock Sample Name)	Latitude	Longitude	Mineral Identification <sup>1</sup>		MTMF Mapping Result
			Field SWIR Reflectance Spectra	Sample Verification	
Prospect I					
1	43°42'13.32"	106°17'43"	Dck, kln		Kaolin group
2	43°42'13.79"	106°17'42.76"	Dck, sme		Alunite
3	43°42'16.73"	106°17'41.71"	Na-alu ( $X_{Na} = 0.81$ ), dck, Kln		Kaolin group
4	43°42'18.29"	106°17'41.35"	K-alu ( $X_{Na} = 0.09$ ), dck		Kaolin group
5	43°42'18.23"	106°17'41.32"	K-alu ( $X_{Na} = 0.09$ ), dck		Kaolin group
6	43°42'18.47"	106°17'41.38"	Dck, kln		Kaolin group
7 (TS108A, B)	43°42'22.75"	106°17'38.19"	Ilt ( $H_2O/Al-OH = 0.97$ ; $Al^{oct} = 1.684$ )	XRD A: ab, qz, or, ms, hem XRD B: ab, qz, or, chl, epi, ilt/sme	Unclassified
8	43°42'23.16"	106°17'35.31"	Dck, kln		Kaolin group
9	43°42'27.84"	106°17'29.65"	K-alu ( $X_{Na} = 0.09$ ), dck		Alunite
10	43°42'34.34"	106°17'20.42"	K-alu ( $X_{Na} = 0.09$ )		Alunite
11	43°42'34.37"	106°17'20.33"	K-alu ( $X_{Na} = 0.09$ )		Alunite
12	43°42'11.83"	106°17'44.62"	Dck, kln		Kaolin group
13	43°42'12.09"	106°17'44.52"	Dck, kln		Alunite
14	43°42'12.39"	106°17'44.37"	K-Na-alu ( $X_{Na} = 0.32$ )		Alunite
15	43°42'12.79"	106°17'44.06"	Dck, kln		Kaolin group
16	43°42'13.08"	106°17'43.49"	Na-alu ( $X_{Na} = 0.81$ ), dck, Kln		Alunite + kaolin group
17	43°42'13.65"	106°17'43.60"	Dck		Kaolin group
18	43°42'13.32"	106°17'43.02"	Dck, kln		Kaolin group
19	43°42'13.31"	106°17'42.67"	K-Na-alu ( $X_{Na} = 0.32$ )		Alunite
20	43°42'13.20"	106°17'42.24"	K-Na-alu ( $X_{Na} = 0.54$ ), dck, Kln		Alunite
21	43°42'12.97"	106°17'42.37"	K-Na-alu ( $X_{Na} = 0.32$ ), dck		Alunite
22	43°42'12.58"	106°17'41.87"	Dck, K-Na-alu ( $X_{Na} = 0.54$ )		Kaolin group
23	43°42'12.55"	106°17'41.89"	K-Na-alu ( $X_{Na} = 0.32$ ), dck, Kln		Alunite
24	43°42'12.34"	106°17'41.42"	K-Na-alu ( $X_{Na} = 0.54$ ), dck, Kln		Kaolin group
25	43°42'12.37"	106°17'41.32"	Na-alu ( $X_{Na} = 0.81$ ), dck, Kln		Kaolin group
26	43°42'13.25"	106°17'41.63"	Na-alu ( $X_{Na} = 0.81$ ), dck, Kln		Alunite
27	43°42'13.45"	106°17'41.77"	Na-alu ( $X_{Na} = 0.81$ ), dck, kln		Alunite

Table A1. Cont.

Field Spectra Sample No. (Rock Sample Name)	Latitude	Longitude	Mineral Identification <sup>1</sup>		MTMF Mapping Result
			Field SWIR Reflectance Spectra	Sample Verification	
28	43°42'13.73"	106°17'42.80"	Dck		Kaolin group
29	43°42'13.84"	106°17'43.10"	Dck		Kaolin group
30	43°42'13.86"	106°17'42.92"	Dck, kln		Kaolin group
31	43°42'14.13"	106°17'42.86"	Dck, kln		Alunite + kaolin group
32	43°42'14.68"	106°17'42.18"	K-Na-alu ( $X_{Na} = 0.32$ )		Alunite
33	43°42'14.48"	106°17'41.69"	Dck, kln		Kaolin group
34	43°42'14.46"	106°17'41.80"	Dck, kln, K-Na-alu ( $X_{Na} = 0.54$ )		Alunite
35	43°42'14.46"	106°17'40.87"	K-alu ( $X_{Na} = 0.09$ ), dck		Alunite
36 (TS104)	43°42'16.54"	106°17'41.82"	K-Na-alu ( $X_{Na} = 0.32$ ), dck, kln	XRD: qz, K-alu, Na-alu, dck, kln	Alunite
37 (TS106A, B)	43°42'16.76"	106°17'41.67"	Dck, kln	XRD A: qz, dck, kln, ant XRD B: qz, dck, kln, hem, ant	Kaolin group
38	43°42'17.09"	106°17'41.57"	Dck		Kaolin group
39	43°42'17.55"	106°17'41.17"	K-Na-alu ( $X_{Na} = 0.32$ ), kln		Kaolin group
40	43°42'17.79"	106°17'41.55"	Dck, kln		Kaolin group
41	43°42'18.17"	106°17'41.43"	Dck, K-alu ( $X_{Na} = 0.09$ ), kln		Kaolin group
42 (TS107)	43°42'18.18"	106°17'41.35"	K-Na-alu ( $X_{Na} = 0.32$ ), dck, kln	XRD: qz, K-alu, Na-alu, dck, kln, ant	Kaolin group
43	43°42'18.32"	106°17'41.73"	Dck, kln		Kaolin group
44	43°42'19.14"	106°17'41.74"	Dck, kln		Kaolin group
45	43°42'19.32"	106°17'41.92"	Dck, kln		Kaolin group
46	43°42'19.28"	106°17'42.62"	Dck, kln		Kaolin group
47	43°42'22.37"	106°17'39.58"	K-Na-alu ( $X_{Na} = 0.32$ ), dck		Alunite
48	43°42'23.22"	106°17'35.34"	Dck, kln		Kaolin group
49	43°42'23.20"	106°17'35.25"	Dck		Unclassified
50	43°42'23.13"	106°17'35.35"	Dck, kln		Kaolin group
51 (TS111)	43°42'27.84"	106°17'26.02"	Dck	XRD: qz, dck, kln	Kaolin group
52	43°42'27.83"	106°17'25.35"	Dck, K-alu ( $X_{Na} = 0.09$ )		Alunite + kaolin group
53	43°42'27.91"	106°17'24.86"	Dck, kln		Kaolin group
54	43°42'28.35"	106°17'23.80"	K-Na-alu ( $X_{Na} = 0.32$ ), dck, kln		Alunite
55	43°42'28.90"	106°17'23.48"	Dck		Alunite
56	43°42'28.85"	106°17'23.37"	Dck		Alunite
57	43°42'28.99"	106°17'23.40"	Dck		Alunite
58	43°42'29.05"	106°17'23.37"	Dck, kln		Alunite

Table A1. Cont.

Field Spectra Sample No. (Rock Sample Name)	Latitude	Longitude	Mineral Identification <sup>1</sup>		MTMF Mapping Result
			Field SWIR Reflectance Spectra	Sample Verification	
59	43°42'29.65"	106°17'22.27"	K-alu ( $X_{Na} = 0.09$ ), zeo? <sup>2</sup>		Alunite
60	43°42'29.77"	106°17'21.66"	K-alu ( $X_{Na} = 0.09$ )		Alunite
61	43°42'29.72"	106°17'21.61"	K-alu ( $X_{Na} = 0.09$ )		Alunite
62	43°42'30.14"	106°17'23.40"	K-alu ( $X_{Na} = 0.09$ )		Alunite
63	43°42'30.80"	106°17'21.49"	K-alu ( $X_{Na} = 0.09$ ), dck		Alunite
64	43°42'31.54"	106°17'21.31"	K-alu ( $X_{Na} = 0.09$ ), dck, kln		Alunite
65 (TS112)	43°42'32.20"	106°17'20.89"	Dck, kln	XRD: qz, kln, dck, cal	Alunite + kaolin group
66	43°42'32.11"	106°17'20.80	Dck, kln		Alunite
67	43°42'33.19"	106°17'20.62"	Dck, kln		Alunite + kaolin group
68	43°42'33.50"	106°17'20.73"	K-alu ( $X_{Na} = 0.09$ )		Alunite
69	43°42'34"	106°17'20.68"	Dck, kln		Alunite
70 (TS113)	43°42'34.26"	106°17'20.45"	K-alu ( $X_{Na} = 0.09$ ), dck, kln	XRD: K-alu, qz, ant	Alunite
71	43°42'35.14"	106°17'20.04	K-alu ( $X_{Na} = 0.09$ )		Alunite
72 (TS137)	43°42'35.87"	106°17'19.50"	Dck, kln	XRD: qz, dck, kln, gp, cal	Alunite + kaolin group
73	43°42'36.29"	106°17'18.68"	K-alu ( $X_{Na} = 0.09$ )		Alunite + kaolin group
74	43°42'36.10"	106°17'17.48"	Dck, kln		Kaolin group
75 (TS138)	43°42'36.77"	106°17'16.41"	Dck, kln	XRD: qz, dck, kln, prl, Na-alu, ant	Alunite + kaolin group
76	43°42'36.97"	106°17'16.19	Dck, kln		Alunite + kaolin group
77	43°42'37.05"	106°17'15.23"	Dck, kln		Kaolin group
78	43°42'37.04"	106°17'15.24"	Dck, kln		Kaolin group
79	43°42'37.15"	106°17'15.59"	Dck, kln		Alunite + kaolin group
80	43°42'37.62"	106°17'15.82"	Dck, kln		Alunite + kaolin group
81	43°42'37.52"	106°17'15.94	Dck, kln		Alunite + kaolin group
82	43°42'38.07"	106°17'16.28"	Kln, dck		Alunite + kaolin group
83	43°42'38.26"	106°17'16.78"	Dck, kln		Kaolin group
84	43°42'38.41"	106°17'17.18"	Dck, kln		Kaolin group
85	43°42'38.42"	106°17'17.17"	Dck		Kaolin group
86	43°42'38.57"	106°17'16.02	Dck		Alunite + kaolin group
87	43°42'37.95"	106°17'14.30"	Dck		Kaolin group

Table A1. Cont.

Field Spectra Sample No. (Rock Sample Name)	Latitude	Longitude	Mineral Identification <sup>1</sup>		MTMF Mapping Result
			Field SWIR Reflectance Spectra	Sample Verification	
88	43°42'37.92"	106°17'14.03"	K-alu ( $X_{Na} = 0.09$ )		Alunite + kaolin group
89	43°42'37.94"	106°17'13.97"	Dck, kln		Alunite + kaolin group
90 (TS139)	43°42'37.98"	106°17'13.56"	Dck, kln	XRD: kln, dck, qz, Na-alu	Kaolin group
91	43°42'37.83"	106°17'13.41	Dck, kln		Kaolin group
92	43°42'38.30"	106°17'13.32"	Dck, kln		Kaolin group
93	43°42'38.31"	106°17'13.36"	Dck		Kaolin group
94	43°42'38.53"	106°17'13.60"	Dck		Kaolin group
95	43°42'38.58"	106°17'13.59"	Dck		Kaolin group
96	43°42'38.72"	106°17'13.79	Dck		Kaolin group
97	43°42'38.95"	106°17'13.47"	K-alu ( $X_{Na} = 0.09$ ), dck		Alunite
98	43°42'39.59"	106°17'13.75"	Dck, kln		Kaolin group
99	43°42'40.11"	106°17'14.36"	K-alu ( $X_{Na} = 0.09$ )		Alunite
100 (TS140A, B)	43°42'40.10"	106°17'14.34"	K-alu ( $X_{Na} = 0.09$ )	XRD A: K-alu, qz XRD B: K-alu, qz	Alunite
101	43°42'40.01"	106°17'14.48	K-alu ( $X_{Na} = 0.09$ )		Alunite
102	43°42'40.15"	106°17'14.49"	K-alu ( $X_{Na} = 0.09$ )		Alunite
103	43°42'40.97"	106°17'14.49"	Dck		Kaolin group
104	43°42'41.66"	106°17'13.88"	Dck, kln		Kaolin group
105	43°42'40.71"	106°17'41.36"	Sme ( $H_2O/Al-OH = 0.73$ )		NH <sub>4</sub> -illite
106	43°42'41.97"	106°17'42.08	Budd ± ilt		Buddingtonite
107	43°42'42.73"	106°17'42.39"	Budd, ilt-sme ( $Al^{oct} = 1.875$ )		Buddingtonite
108	43°42'42.70"	106°17'43.11"	Ilt-sme ( $H_2O/Al-OH = 0.88$ ; $Al^{oct} = 1.684$ )		Buddingtonite
109	43°42'42.64"	106°17'43.20"	Budd		Buddingtonite
110	43°42'39.89"	106°17'44.76"	Ilt-sme ( $H_2O/Al-OH = 0.96$ ; $Al^{oct} = 1.875$ )		Illite/smectite
111	43°42'39.49"	106°17'45.16	Sme ( $H_2O/Al-OH = 0.69$ )		Buddingtonite
112 (TS143)	43°42'39.88"	106°17'44.74"	NH <sub>4</sub> -ilt	XRD: qz, fl, ms, or	NH <sub>4</sub> -illite
113	43°42'39.60"	106°17'44.78"	Sme ( $H_2O/Al-OH = 0.63$ )		Buddingtonite
114	43°42'36.15"	106°17'51.11"	Dck		Kaolin group
115	43°42'36.25"	106°17'51.29"	Dck, kln		Kaolin group
116	43°42'36.30"	106°17'51.33"	Dck		Kaolin group
117	43°42'36.25"	106°17'53.64"	Sme ( $H_2O/Al-OH = 0.72$ )		Illite/smectite
Prospect II					
118	43°43'16.47"	106°18'37.51"	Dck, kln, Gp		Kaolin group
119	43°43'17.33"	106°18'36.41"	Dck, kln		Kaolin group

Table A1. Cont.

Field Spectra Sample No. (Rock Sample Name)	Latitude	Longitude	Mineral Identification <sup>1</sup>		MTMF Mapping Result
			Field SWIR Reflectance Spectra	Sample Verification	
120	43°43'18.08"	106°18'35.78"	Dck, kln		Kaolin group
121	43°43'18.31"	106°18'35.27"	Dck, kln		Kaolin group
122	43°43'18.34"	106°18'35.31"	Dck, kln		Kaolin group
123	43°43'18.37"	106°18'35.30"	Dck, kln		Kaolin group
124 (TS128A, B)	43°43'18.06"	106°18'39.72"	Ilt (H <sub>2</sub> O/Al-OH = 1.04; Al <sup>oct</sup> = 1.684)	XRD A: qz, ab, or, ms XRD B: qz, or, ms, ab	Illite/smectite
125	43°43'18.06"	106°18'39.63"	Ilt-sme (H <sub>2</sub> O/Al-OH = 0.86; Al <sup>oct</sup> = 1.684)		Illite/smectite
126	43°43'18.05"	106°18'39.60"	Ilt-sme (H <sub>2</sub> O/Al-OH = 0.83; Al <sup>oct</sup> = 1.684)		Illite/smectite
127 (TS129)	43°43'17.36"	106°18'38.94"	Dck, kln	XRD: dck, kln, qz, Na-alu	Alunite + kaolin group
128	43°43'17.33"	106°18'38.81"	Dck, kln		Alunite + kaolin group
129	43°43'17.27"	106°18'38.83"	Dck, kln		Alunite + kaolin group
130	43°43'17.25"	106°18'36.13"	Dck, kln		Kaolin group
131	43°43'17.90"	106°18'35.89"	Ilt-sme (H <sub>2</sub> O/Al-OH = 0.83; Al <sup>oct</sup> = 1.493)		Kaolin group
132	43°43'17.93"	106°18'36.05"	Zeo? <sup>2</sup>		Kaolin group
133	43°43'17.96"	106°18'35.97"	Zeo?		Kaolin group
134 (TS131A, B)	43°43'18.07"	106°18'35.72"	Dck, kln	XRD A: dck, kln, qz XRD B: qz, dck, kln, hem, cal	Kaolin group
135	43°43'18.11"	106°18'35.70"	Dck, kln		Kaolin group
136	43°43'18.36"	106°18'34.48"	Dck		Kaolin group
137 (TS132)	43°43'18.52"	106°18'33.35"	K-alu (X <sub>Na</sub> = 0.09), dck, kln	XRD: qz, dck, kln, K-alu, hem	Alunite
138 (TS133)	43°43'17.34"	106°18'18.15"	Ilt-sme (H <sub>2</sub> O/Al-OH = 0.83; Al <sup>oct</sup> = 1.684)	XRD: qz	Illite/smectite
139	43°43'16.95"	106°18'16.85"	Ilt-sme (H <sub>2</sub> O/Al-OH = 0.80; Al <sup>oct</sup> = 1.684)		Smectite
140	43°43'16.88"	106°18'16.09"	Ilt-sme (H <sub>2</sub> O/Al-OH = 0.77; Al <sup>oct</sup> = 1.684)		Smectite
141	43°43'17.08"	106°18'14.64"	Ilt-sme (H <sub>2</sub> O/Al-OH = 0.82; Al <sup>oct</sup> = 1.684)		Smectite
142 (TS134)	43°43'17.27"	106°18'13.34"	Ilt-sme (H <sub>2</sub> O/Al-OH = 0.92; Al <sup>oct</sup> = 1.684)	XRD: ab, qz, or	Smectite
143	43°43'17.43"	106°18'11.28"	Sme (H <sub>2</sub> O/Al-OH = 0.70)		Smectite
144	43°43'17.49"	106°18'10.61"	Ilt-sme (H <sub>2</sub> O/Al-OH = 0.81; Al <sup>oct</sup> = 1.684)		Illite/smectite

Table A1. Cont.

Field Spectra Sample No. (Rock Sample Name)	Latitude	Longitude	Mineral Identification <sup>1</sup>		MTMF Mapping Result
			Field SWIR Reflectance Spectra	Sample Verification	
145 (TS136)	43°43'19.59"	106°18'2.58"	Dck	XRD: dck, kln, qz,	Kaolin group
146	43°43'19.68"	106°18'2.53"	Dck, K-alu ( $X_{Na} = 0.09$ )		Kaolin group
147	43°43'19.70"	106°18'2.52"	Dck, K-alu ( $X_{Na} = 0.09$ )		Kaolin group
148	43°43'19.74"	106°18'2.44"	Dck		Kaolin group
149	43°43'19.41"	106°18'1.99"	Dck, kln		Kaolin group
150	43°43'19.21"	106°18'1.73"	Dck		Kaolin group
151	43°43'19.26"	106°18'1.78"	Dck, kln		Kaolin group
152	43°43'19.79"	106°18'1.02"	Dck, kln		Illite/smectite
153	43°43'19.82"	106°18'1"	Dck, kln		Illite/smectite
Prospect III					
154	43°43'20.91"	106°21'15.05"	Kln (PXL)		Unclassified
155	43°43'20.90"	106°21'15.07"	Dck, sme		Unclassified
156	43°43'22.36"	106°21'14.45"	Kln (WXL), sme		Kaolin group
157	43°43'22.41"	106°21'14.47"	Sme ( $H_2O/Al-OH = 0.74$ )		Kaolin group
158	43°43'23.35"	106°21'14.37"	Kln (WXL)		Kaolin group
159	43°43'23.50"	106°21'14.77"	Kln (WXL)		Kaolin group
160	43°43'23.80"	106°21'14.97"	Kln (WXL)		Kaolin group
161	43°43'27.62"	106°21'18.12"	Kln (WXL), K-alu ( $X_{Na} = 0.09$ )		Alunite + kaolin group
162	43°43'27.60"	106°21'18.56"	Kln (WXL)		Alunite + kaolin group
163 (TS116A, B)	43°43'27.63"	106°21'18.57"	Kln (WXL), K-alu ( $X_{Na} = 0.09$ )	XRD A: qz, kln, dck, K-alu, cal XRD B: qz, kln, dck, K-alu	Alunite + kaolin group
164	43°43'27.63"	106°21'18.59"	K-alu ( $X_{Na} = 0.09$ ), kln		Alunite + kaolin group
165	43°43'27.61"	106°21'18.58"	Kln (WXL)		Alunite + kaolin group
166 (TS117)	43°43'27.30"	106°21'19.11"	Kln (WXL)	XRD: qz, kln, dck, Na-alu, ant	Alunite + kaolin group
167	43°43'27.29"	106°21'19.10"	Kln (WXL)		Alunite + kaolin group
168	43°43'26.80"	106°21'19.96"	Kln (WXL)		Alunite + kaolin group
169 (TS118)	43°43'26.83"	106°21'20.02"	Kln (WXL)	XRD: kln, dck, qz, K-alu, ant	Alunite + kaolin group
170	43°43'27.64"	106°21'21.88"	K-alu ( $X_{Na} = 0.09$ ), kln		Alunite + kaolin group
171	43°43'27.65"	106°21'22.24"	K-alu ( $X_{Na} = 0.09$ ), kln		Alunite + kaolin group

Table A1. Cont.

Field Spectra Sample No. (Rock Sample Name)	Latitude	Longitude	Mineral Identification <sup>1</sup>		MTMF Mapping Result
			Field SWIR Reflectance Spectra	Sample Verification	
172 (TS119)	43°43'27.17"	106°21'22.95"	Kln (WXL)	XRD: qz, kln, dck, Na-alu, ant	Kaolin group
173	43°43'26.10"	106°21'23.05"	Kln (WXL)		Kaolin group
174	43°43'25.96"	106°21'26.08"	Kln (PXL)		Kaolin group
175 (TS121)	43°43'26.02"	106°21'26.02"	Kln (PXL)	XRD: kln, dck, qz, Na-alu, ant	Kaolin group
176	43°43'26.49"	106°21'26.12"	Kln (WXL)		Kaolin group
177	43°43'26.40"	106°21'26.20"	Kln (PXL)		Kaolin group
178	43°43'26.46"	106°21'26.67"	Dck		Kaolin group
179	43°43'27.96"	106°21'27.52"	Kln (PXL)		Kaolin group
180 (TS123)	43°43'29.97"	106°21'28.85"	Kln (PXL), dck	XRD: kln, dck, qz, K-alu, ant	Kaolin group
181	43°43'30.18"	106°21'30.26"	Dck, kln		Kaolin group
182	43°43'30.17"	106°21'30.23"	Dck, kln		Kaolin group
183 (TS125)	43°43'30.24"	106°21'30.74"	Kln (WXL)	XRD: qz, kln, dck, K-alu, ant, gp, cal	Kaolin group
184	43°43'30.50"	106°21'31.14"	Kln (WXL)		Kaolin group
185	43°43'30.97"	106°21'30.76"	K-Na-al ( $X_{Na} = 0.32$ ), kln		Alunite
186	43°43'30.61"	106°21'30.45"	Kln (PXL)		Kaolin group
187	43°43'30.60"	106°21'31.24"	K-Na-al ( $X_{Na} = 0.32$ ), kln		Alunite
188	43°43'30.45"	106°21'30.80"	K-Na-al ( $X_{Na} = 0.32$ ), kln		Alunite + kaolin group
189 (TS126A, B)	43°43'30.60"	106°21'30.59"	Kln (WXL)	XRD A: qz, kln, dck, K-alu, ant XRD B: kln, dck, qz, hem, ant	Kaolin group
190	43°43'30.95"	106°21'33.47"	Dck, kln		Kaolin group
191 (TS127)	43°43'30.81"	106°21'34.29"	Dck, kln	XRD: dck, kln, qz, K-alu, ant, gbs	Kaolin group
192	43°43'30.66"	106°21'34.31"	Dck, kln		Kaolin group

Note: Minerals detected in XRD analysis but not recognized by field SWIR reflectance spectroscopy may be present in small amounts or have no absorption features at the SWIR wavelength (e.g., quartz, hematite, and albite);  $X_{Na}$  = mole fraction of Na in alunite,  $X_{Na}$  calculated using Equation (2) in Section 4.1 for field SWIR reflectance spectra;  $H_2O/Al-OH$  = absorption depth ratio of illite, smectite, and mixed-layered illite-smectite due to water molecular and cation-OH bonds;  $Al^{oct}$  = cation number of Al in the octahedral position of illite compositional series calculated using equation ( $Al^{oct} = (\lambda - 2.293) / -0.05226$  ( $2.194 < \lambda < 2.217 \mu m$ )) suggested by [29] for field spectroscopy measurements. Abbreviations: ab = albite, al = alunite, ant = anatase, budd = buddingtonite, cal = calcite, chl = chlorite, dck = dickite, epi = epistilbite, fl = fluorite, gbs = gibbsite, gp = gypsum, hem = hematite, ilt = illite, ilt/sme = illite-smectite mixed minerals, kln = kaolinite (WXL: well crystallised, PXL: poor crystallised), ms = muscovite,  $NH_4$ -ilt = ammonium illite, or = orthoclase, prl = pyrophyllite, qz = quartz, sme = smectite, zeo = zeolite. <sup>1</sup> In order of abundance. <sup>2</sup> The question mark indicates the uncertainty of the mineral determination.

## References

- Hedenquist, J.W.; Arribas, A.R.; Gonzalez-Urien, E. Exploration for epithermal gold deposits. *Rev. Econ. Geol.* **2000**, *13*, 245–277.
- Sillitoe, R.H. Porphyry copper systems. *Econ. Geol.* **2010**, *105*, 3–41. [[CrossRef](#)]
- Lee, C.-T.A.; Tang, M. How to make porphyry copper deposits. *Earth Planet. Sci. Lett.* **2020**, *529*, 115868. [[CrossRef](#)]
- Ducart, D.F.; Crosta, A.P.; Filho, C.R.S.; Coniglio, J. Alteration mineralogy at the Cerro La Mina epithermal prospect, Patagonia, Argentina: Field mapping, short-wave infrared spectroscopy, and ASTER images. *Econ. Geol.* **2006**, *101*, 981–996. [[CrossRef](#)]

5. Mars, J.C.; Rowan, L.C. Regional mapping of phyllic-and argillic-altered rocks in the Zagros magmatic arc, Iran, using Advanced Spaceborne Thermal Emission and Reflectance Radiometer (ASTER) data and logical operator algorithms. *Geosphere* **2006**, *2*, 161–186. [[CrossRef](#)]
6. Chang, Z.; Hedenquist, J.W.; White, N.C.; Cooke, D.R.; Roach, M.; Deyell, C.L.; Garcia, J.; Gemmell, J.B.; McKnight, S.; Cuison, A.L. Exploration tools for linked porphyry and epithermal deposits: Example from the Mankayan intrusion-centered Cu–Au district, Luzon, Philippines. *Econ. Geol.* **2011**, *106*, 1365–1398. [[CrossRef](#)]
7. Haselwimmer, C.E.; Riley, T.R.; Liu, J.G. Assessing the potential of multispectral remote sensing for lithological mapping on the Antarctic Peninsula: Case study from eastern Adelaide Island, Graham Land. *Antarct. Sci.* **2010**, *22*, 299–318. [[CrossRef](#)]
8. Bedini, E. Mineral mapping in the Kap Simpson complex, central East Greenland, using HyMap and ASTER remote sensing data. *Adv. Space Res.* **2011**, *47*, 60–73. [[CrossRef](#)]
9. Son, Y.S.; Kim, K.E.; Yoon, W.J.; Cho, S.J. Regional mineral mapping of island arc terranes in southeastern Mongolia using multispectral remote sensing data. *Ore Geol. Rev.* **2019**, *113*, 103106. [[CrossRef](#)]
10. Sabins, F.F. Remote sensing for mineral exploration. *Ore Geol. Rev.* **1999**, *14*, 157–183. [[CrossRef](#)]
11. Son, Y.S.; Kang, M.K.; Yoon, Y.J. Lithological and mineralogical survey of the Oyu Tolgoi region, Southeastern Gobi, Mongolia using ASTER reflectance and emissivity data. *Int. J. Appl. Earth Obs. Geoinf.* **2014**, *26*, 205–216. [[CrossRef](#)]
12. Graham, G.E.; Kokaly, R.F.; Kelley, K.D.; Hoefen, T.M.; Johnson, M.R.; Hubbard, B.E. Application of imaging spectroscopy for mineral exploration in Alaska: A study over porphyry Cu deposits in the Eastern Alaska Range. *Econ. Geol.* **2018**, *113*, 489–510. [[CrossRef](#)]
13. Van der Meer, F.D.; van der Werff, H.M.A.; van Ruitenbeek, F.J.A.; Hecker, C.A.; Bakker, W.H.; Noomen, M.F.; van der Meijde, M.; Carranza, E.J.M. Multi- and hyper-spectral geologic remote sensing: A review. *Int. J. Appl. Earth Obs. Geoinf.* **2012**, *14*, 112–128. [[CrossRef](#)]
14. Hewson, R.D.; Cudahy, T.J.; Mizuhiko, S.; Ueda, K.; Mauger, A.J. Seamless geological map generation using ASTER in the Broken Hill-Curnamona province of Australia. *Remote Sens. Environ.* **2005**, *99*, 159–172. [[CrossRef](#)]
15. Abrams, M.; Yamaguchi, Y. Twenty years of ASTER contributions to lithologic mapping and mineral exploration. *Remote Sens.* **2019**, *11*, 1394. [[CrossRef](#)]
16. Kruse, F.A.; Perry, S.L. Mineral mapping using simulated worldview-3 short-wave infrared imagery. *Remote Sens.* **2013**, *5*, 2688–2703. [[CrossRef](#)]
17. Mars, J.C.; Rowan, L.C. Spectral assessment of new ASTER SWIR surface reflectance data products for spectroscopic mapping of rocks and minerals. *Remote Sens. Environ.* **2010**, *114*, 2011–2025. [[CrossRef](#)]
18. Biggar, S.F.; Thome, K.T.; MacCorkel, J.T.; D’Amico, J.M. Vicarious calibration of the ASTER SWIR sensor including crosstalk correction. In Proceedings of the SPIE 5882: Earth observing Systems, San Diego, CA, USA, 22 August 2005; p. 588217.
19. Iwasaki, A.; Tonooka, H. Validation of a crosstalk correction algorithm for ASTER/SWIR. *IEEE Trans. Geosci. Remote Sens.* **2005**, *43*, 2747–2751. [[CrossRef](#)]
20. Ye, B.; Tian, S.H.; Ge, J.; Sun, Y. Assessment of WorldView-3 data for lithological mapping. *Remote Sens.* **2017**, *9*, 1132. [[CrossRef](#)]
21. Kruse, F.A.; Baugh, M.W.; Perry, S.L. Validation of DigitalGlobe Worldview-3 earth imaging satellite shortwave infrared bands for mineral mapping. *J. Appl. Remote Sens.* **2015**, *9*, 1–18. [[CrossRef](#)]
22. Mars, J.C. Mineral and lithologic mapping capability of WorldView 3 data at Mountain Pass, California, using true and false-color composite images, band ratios, and logical operator algorithms. *Econ. Geol.* **2018**, *113*, 1587–1601. [[CrossRef](#)]
23. Salehi, T.; Tangestani, M.H. Large-scale mapping of iron oxide and hydroxide minerals of Zefreh porphyry copper deposit, using WorldView-3 VNIR data in the northeastern Isfahan, Iran. *Int. J. Appl. Earth Obs. Geoinf.* **2018**, *73*, 156–169. [[CrossRef](#)]
24. Bedini, E. Application of WorldView-3 imagery and ASTER TIR data to map alteration minerals associated with the Rodalquilar gold deposits, southeast Spain. *Adv. Space Res.* **2019**, *63*, 3346–3357. [[CrossRef](#)]
25. Thompson, S.; Fueten, F.; Bockus, D. Mineral identification using artificial neural networks and the rotating polarizer stage. *Comput. Geosci.* **2001**, *27*, 1081–1089. [[CrossRef](#)]
26. Yousefi, B.; Sojasi, S.; Castanedo, C.I.; Maldague, X.P.; Beaudoin, G.; Chamberland, M. Comparison assessment of low rank sparse-PCA based-clustering/classification for automatic mineral identification in long wave infrared hyperspectral imagery. *Infrared Phys. Technol.* **2018**, *93*, 103–111. [[CrossRef](#)]
27. Yousefi, B.; Castanedo, C.I.; Maldague, X.P.; Beaudoin, G. Assessing the reliability of an automated system for mineral identification using LWIR Hyperspectral Infrared imagery. *Miner. Eng.* **2020**, *155*, 106409. [[CrossRef](#)]
28. Hu, B.; Xu, Y.Y.; Wan, B.; Wu, X.C.; Yi, G.H. Hydrothermally altered mineral mapping using synthetic application of Sentinel-2A MSI, ASTER and Hyperion data in the Duolong area, Tibetan Plateau, China. *Ore Geol. Rev.* **2018**, *101*, 384–397. [[CrossRef](#)]
29. Watanabe, Y.; Stein, H.J. Re-Os ages for the Erdenet and Tsagaan Suvarga porphyry Cu-Mo deposits, Mongolia, and tectonic implications. *Econ. Geol.* **2000**, *95*, 1537–1542. [[CrossRef](#)]
30. Perello, J.; Cox, D.; Garamjav, D.; Sanjdori, S.; Diakov, S.; Schissel, D.; Munkhbat, T.O.; Oyun, G.; Oyu Tolgoi, M. Siluro-Devonian porphyry Cu-Au-(Mo) and high-sulfidation Cu mineralization with a Cretaceous chalcocite blanket. *Econ. Geol.* **2001**, *96*, 1407–1428. [[CrossRef](#)]
31. Müller, A.; Herrington, R.; Armstrong, R.; Seltmann, R.; Kirwin, D.J.; Stenina, N.G.; Kronz, A. Trace elements and cathodoluminescence of quartz in stockwork veins of Mongolian porphyry-style deposits. *Miner. Depos.* **2010**, *45*, 707–727. [[CrossRef](#)]

32. Batkhishig, B.; Noriyoshi, T.; Greg, B. Magmatism of the Shuteen Complex and Carboniferous subduction of the Gurvansaikhan terrane, South Mongolia. *J. Asian Earth Sci.* **2010**, *37*, 399–411. [[CrossRef](#)]
33. Swayze, G.A.; Clark, R.N.; Goetz, A.F.; Livo, K.E.; Breit, G.N.; Kruse, F.A.; Sutley, S.J.; Snee, L.W.; Lowers, H.A.; Post, J.L.; et al. Mapping advanced argillic alteration at cuprite, Nevada, using imaging spectroscopy. *Econ. Geol.* **2014**, *109*, 1179–1221. [[CrossRef](#)]
34. Jamiyandorj, O.; Zoljargal, A. *Geological Map of Mongolia, Ikh Luusiin Uul Sheet K-48-V (1:200,000 Scale)*; Mineral Resources Authority of Mongolia: Ulaanbaatar, Mongolia, 2010.
35. Baugh, W.M.; Kruse, F.A.; Atkinson, W.W. Quantitative geochemical mapping of ammonium minerals in the southern cedar mountains, Nevada, using the airborne visible/infrared imaging spectrometer (AVIRIS). *Remote Sens. Environ.* **1998**, *65*, 292–308. [[CrossRef](#)]
36. Yang, K.; Browne, P.R.L.; Huntington, J.F.; Walshe, J.L. Characterising the hydrothermal alteration of the Broadlands–Ohaaki geothermal system, New Zealand, using short-wave infrared spectroscopy. *J. Volcanol. Geotherm. Res.* **2001**, *106*, 53–65. [[CrossRef](#)]
37. Soechting, W.; Rubinstein, N.; Godeas, M. Identification of ammonium bearing minerals by shortwave infrared reflectance spectroscopy at the Esquel gold deposit, Argentina. *Econ. Geol.* **2008**, *103*, 865–869. [[CrossRef](#)]
38. Canet, C.; Hernández-Cruz, B.; Jiménez-Franco, A.; Pi, T.; Peláez, B.; Villanueva-Estrada, R.E.; Alfonso, P.; González-Partida, E.; Salinas, S. Combining ammonium mapping and short-wave infrared (SWIR) reflectance spectroscopy to constrain a model of hydrothermal alteration for the Acoculco geothermal zone, Eastern Mexico. *Geothermics* **2015**, *53*, 154–165. [[CrossRef](#)]
39. Kokaly, R.F.; Clark, R.N.; Swayze, G.A.; Livo, K.E.; Hoefen, T.M.; Pearson, N.C.; Wise, R.A.; Benzel, W.M.; Lowers, H.A.; Driscoll, R.L.; et al. *USGS Spectral Library Version 7: U.S. Geological Survey Data Series 1035*; U.S. Geological Survey: Reston, VA, USA, 2017; 61p.
40. Simpson, M.P.; Rae, A.J. Short-wave Infrared (SWIR) reflectance spectrometric characterisation of clays from geothermal systems of the Taupo volcanic zone, New Zealand. *Geothermics* **2018**, *73*, 74–90. [[CrossRef](#)]
41. Congalton, R.G.; Green, K. *Assessing the Accuracy of Remotely Sensed Data: Principles and Practices*, 2nd ed.; CRC/Taylor & Francis: Boca Raton, FL, USA, 2009; ISBN 978-1-4200-5512-2.
42. Kuester, M.A. *Radiometric Use of WV-3 Imagery*; Technical Note; DigitalGlobe: Westminster, CO, USA, 2016.
43. Kuester, M.; Ochoa, T. *Improvements in Calibration, and Validation of the Absolute Radiometric Response of MAXAR Earth-Observing Sensors*; Joint Agency Commercial Imagery Evaluation (JACIE) Workshop: Reston, VA, USA, 2019.
44. Kruse, F.A. Use of airborne imaging spectrometer data to map minerals associated with hydrothermally altered rocks in the northern grapevine mountains, Nevada, and California. *Remote Sens. Environ.* **1988**, *24*, 31–51. [[CrossRef](#)]
45. Ben-Dor, E.; Kruse, F.A. The relationship between the size of spatial subsets of GER 63 channel scanner data and the quality of the Internal Average Relative Reflectance (IARR) atmospheric correction technique. *Int. J. Remote Sens.* **1994**, *15*, 683–690. [[CrossRef](#)]
46. Bishop, C.A.; Liu, J.G.; Mason, P.J. Hyperspectral remote sensing for mineral exploration in Pulang, Yunnan Province, China. *Int. J. Remote Sens.* **2011**, *32*, 2409–2426. [[CrossRef](#)]
47. Guha, A.; Vinod Kumar, K.; Porwal, A.; Rani, K.; Singaraju, V.; Singh, R.P.; Khandelwal, M.K.; Raju, P.V.; Diwakar, P.G. Reflectance spectroscopy and ASTER based mapping of rock-phosphate in parts of Paleoproterozoic sequences of Aravalli Group of rocks, Rajasthan, India. *Ore Geol. Rev.* **2019**, *108*, 73–87. [[CrossRef](#)]
48. Gillespie, A.R.; Kahle, A.B.; Walker, R.E. Color enhancement of highly correlated images: I. Decorrelation and HIS contrast stretches. *Remote Sens. Environ.* **1986**, *20*, 209–235. [[CrossRef](#)]
49. Aslett, Z.; Taranik, J.V.; Riley, D.N. Mapping rock forming minerals at Boundary Canyon, Death Valley National Park, California, using aerial SEBASS thermal infrared hyperspectral image data. *Int. J. Appl. Earth Obs. Geoinf.* **2018**, *64*, 326–339. [[CrossRef](#)]
50. Crowley, J.K.; Brickey, D.W.; Rowan, L.C. Airborne imaging spectrometer data of the Ruby Mountains, Montana: Mineral discrimination using relative absorption band-depth images. *Remote Sens. Environ.* **1989**, *29*, 121–134. [[CrossRef](#)]
51. Rowan, L.C.; Mars, J.C. Lithologic mapping in the Mountain Pass, California area using Advanced Spaceborne Thermal Emission and Reflectance Radiometer (ASTER) data. *Remote Sens. Environ.* **2003**, *84*, 350–366. [[CrossRef](#)]
52. Ninomiya, Y.; Fu, B.; Cudahy, T.J. Detecting lithology with Advanced Spaceborne Thermal Emission and Reflectance Radiometer (ASTER) multispectral thermal infrared radiance-at-sensor data. *Remote Sens. Environ.* **2005**, *99*, 127–139. [[CrossRef](#)]
53. Boardman, J.W.; Kruse, F.A. Analysis of imaging spectrometer data using N-Dimensional geometry and a mixture-tuned matched filtering approach. *IEEE Trans. Geosci. Remote Sens.* **2011**, *49*, 4138–4152. [[CrossRef](#)]
54. Carrino, T.A.; Crosta, A.P.; Toledo, C.L.B.; Silva, A.M. Hyperspectral remote sensing applied to mineral exploration in southern Peru: A multiple data integration approach in the Chapi Chiara gold prospect. *Int. J. Appl. Earth Obs. Geoinf.* **2018**, *64*, 287–300. [[CrossRef](#)]
55. Salles, R.D.R.; de Souza Filho, C.R.; Cudahy, T.; Vicente, L.E.; Monteiro, L.V.S. Hyperspectral remote sensing applied to uranium exploration: A case study at the Mary Kathleen metamorphic-hydrothermal U-REE deposit, NW, Queensland, Australia. *J. Geochem. Explor.* **2016**, *179*, 36–50. [[CrossRef](#)]
56. Reyes, A.G. Petrology of Philippine geothermal systems and the application of alteration mineralogy to their assessment. *J. Volcanol. Geotherm. Res.* **1990**, *43*, 279–309. [[CrossRef](#)]
57. Solomon, G.C.; Rossman, G.R.  $\text{NH}_4^+$  in pegmatitic feldspars from the southern Black Hills, South Dakota. *Am. Mineral.* **1988**, *73*, 818–821.
58. Stoffregen, R.E.; Cygan, G.L. An experimental study of Na-K exchange between alunite and aqueous sulfate solutions. *Am. Mineral.* **1990**, *75*, 209–220.

59. Deyell, C.L.; Dipple, G.M. Equilibrium mineral-fluid calculations and their application to the solid solution between alunite and natroalunite in the El Indio-Pascua belt of Chile and Argentina. *Chem. Geol.* **2005**, *215*, 219–234. [[CrossRef](#)]
60. Cudahy, T.J. Mineral mapping for exploration: An Australian journey of evolving spectral sensing technologies and industry collaboration. *Geosciences* **2016**, *6*, 52. [[CrossRef](#)]
61. Gustafson, L.B.; Vidal, C.E.; Pinto, R.; Noble, D.C. Porphyry-epithermal transition, Cajamarca region, northern Peru. *Soc. Econ. Geol. Spec. Publ.* **2004**, *11*, 279–299.
62. Harraden, C.L.; McNulty, B.A.; Gregory, M.J.; Lang, J.R. Shortwave infrared spectral analysis of hydrothermal alteration associated with the Pebble porphyry copper-gold-molybdenum deposit, Iliamna, Alaska. *Econ. Geol.* **2013**, *108*, 483–494. [[CrossRef](#)]
63. Krohn, M.D.; Altaner, S.P. Near-infrared detection of ammonium minerals. *Geophysics* **1987**, *52*, 924–930. [[CrossRef](#)]
64. Queralt, I.; Kanazirski, M.; Gorova, M. Adularia–sericite type wallrock alteration at the Maria Josefa goldmine: An example of low sulfidation epithermal ore deposit within the volcanic Rodalquilar Caldera (SE, Spain). *Acta Geol. Hispánica* **1995**, *30*, 91–100.